

# Understanding Classifier-Free Guidance: High-Dimensional Theory and Non-Linear Generalizations

Krunoslav Lehman Pavasovic<sup>1,2</sup>, Jakob Verbeek<sup>1</sup>, Giulio Biroli<sup>2,†</sup>, Marc Mezard<sup>3,†</sup>

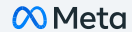
<sup>1</sup>FAIR at Meta, <sup>2</sup>École Normale Supérieure, Paris, <sup>3</sup>Bocconi University, Milan

<sup>†</sup>Joint last author

Recent studies have raised concerns about the effectiveness of Classifier-Free Guidance (CFG), indicating that in low-dimensional settings, it can lead to overshooting the target distribution and reducing sample diversity. In this work, we demonstrate that in infinite and sufficiently high-dimensional contexts CFG effectively reproduces the target distribution, revealing a “blessing-of-dimensionality” result. Additionally, we explore finite-dimensional effects, precisely characterizing overshoot and variance reduction. Based on our analysis, we introduce non-linear generalizations of CFG. Through numerical simulations on Gaussian mixtures and experiments on class-conditional and text-to-image diffusion models we validate our analysis and show that our non-linear CFG offers improved flexibility and generation quality without additional computation cost.

**Date:** February 13, 2025

**Correspondence:** Krunoslav Lehman Pavasovic at [krunolp@meta.com](mailto:krunolp@meta.com)



## 1 Introduction

Diffusion models (Sohl-Dickstein et al., 2015; Song and Ermon, 2020; Ho et al., 2020) have become the state-of-the-art algorithms to generate high-quality images, audio and video. By simulating Ornstein-Uhlenbeck Langevin dynamics, noise is first progressively added to data until it becomes completely random. Diffusion models then learn to reverse this process and generate new samples through a time-reversed Langevin equation. This backward evolution is steered by a force, the score, that is estimated from the data. An important task for diffusion models is generating data conditioned on a label, e.g., in text-to-image generation, on a textual description which allows the model to generate images that match the content of the description. This can be achieved through the concept of guidance (Dhariwal and Nichol, 2021; Ho and Salimans, 2022). This approach allows the model to generate more specific outputs that align with user intentions or desired properties, rather than producing generic samples from the model of the data distribution. Guidance allows control over the generative sampling process, making it possible to create outputs with higher fidelity and relevance to the input criteria.

The first form of guidance introduced was classifier guidance (Song et al., 2020a; Dhariwal and Nichol, 2021). In this approach, one learns scores conditioned on class labels using a classifier that estimates the probability that a given noised image corresponds to the given label. This technique allows for precise control over the attributes of the generated outputs, enhancing their alignment with specific categories. However, the reliance on a pre-trained classifier can be computationally expensive and may introduce biases inherent to the classifier itself.

Classifier-Free Guidance (CFG) (Ho and Salimans, 2022) was developed as an alternative to overcome these challenges, and was quickly adopted as a standard technique in state-of-the-art diffusion models such as GLIDE (Nichol et al., 2021), DALL-E 3 (Betker et al., 2023), Imagen (Saharia et al., 2022), and EMU (Dai et al., 2023), as well as flow matching based models (Esser et al., 2024). CFG eliminates the need for an external classifier by training the diffusion model to conditionally generate samples based on class labels/textual prompts directly. During training, the model learns to produce both class-conditional and unconditional samples. The score used in classifier-free guidance, however, *is not* the one guaranteed to give the target distribution. Instead, one adds to the latter an extra term whose role is to better guide the backward process toward the desired labeled data.

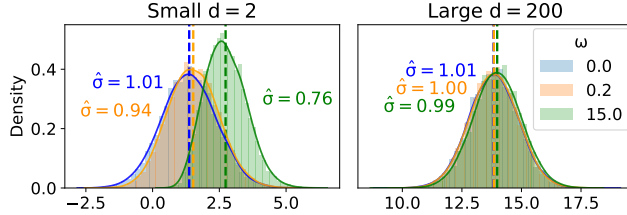


**Figure 1 CFG only overshoots in low dimensions.** Model: mixture of two Gaussians (only one component shown) with dimension  $d = 2$  (left) and  $d = 200$  (right), centered in  $\pm\vec{m}$  and variance  $\sigma^2 = 1$ ,  $\omega \in \{0, 0.2, 15\}$ , see Eq. (10). We show the histograms of  $q(t=0) = \vec{x} \cdot \vec{m}/|\vec{m}|$ , the generated samples projected onto the normalized mean vector  $\vec{m}$  obtained with backward diffusion with 10,000 trajectories. The guidance strength is given by  $\omega$ , and  $\omega = 0$  corresponds to sampling without CFG. For  $d = 2$ , CFG generates a distribution with larger magnitude mean (dashed vertical line) and smaller variance. This effect diminishes when the dimension increases: for  $d = 200$  it is practically absent.

CFG sampling of diffusion models is a surprising procedure in many ways. On the one hand, it lacks a theoretical foundation, and it has been proven wrong in simple examples like one-dimensional Gaussian mixtures, as it leads to a wrong target distribution (Chidambaram et al., 2024). In fact, several recent theoretical studies (Wu et al., 2024; Xia et al., 2024; Bradley and Nakkiran, 2024) explored this phenomenon in low-dimensional settings, concluding that CFG is ineffective and may result in diffusion *overshooting* the target distribution, as well as *shrinking* the variance. The left panel of Figure 1 shows an example for a two-dimensional Gaussian mixture. On the other hand, CFG is beneficial in real applications, and used to generate high-quality samples that are consistent with the input conditioning. Understanding why CFG is wrong in theory but good in practice is the riddle that we address in this work.

*Our Contributions.* We show through theoretical arguments and empirical results that the high-dimensionality of the data, which results in the emergence of distinct dynamical regimes, allows CFG to correctly reproduce the target distribution, as shown in the right panel of Figure 1 for a 200-dimensional Gaussian mixture defined in Section 4. The conditions are the same as for the case of  $d = 2$  (left panel) which instead exhibits overshooting of the mean and variance shrinking. Based on these theoretical results, we propose a more general class of non-linear CFG schemes. We apply these to class-conditional and text-to-image diffusion models, and show that these general CFGs are beneficial in practice in terms of image quality and diversity.

Our contributions are therefore two-fold:

**I.** We explain the correctness of CFG for high-dimensional data by leveraging the emergence of separate dynamical regimes in the backward diffusion process (Biroli et al., 2024). CFG acts in the first regime associated to the formation of classes and to symmetry-breaking (Biroli and Mézard, 2023; Raya and Ambrogioni, 2024) by guiding faster toward the desired class, but it does not have any effect in the second regime where the generation conditioned to the class actually takes place. We provide a thorough theoretical analysis of this blessing-of-dimensionality phenomenon for high-dimensional Gaussian mixtures. For lower dimensional data, CFG generates a distribution which has a perturbed mean (with higher magnitude) and a lower variance. We characterize this result exactly for Gaussian mixture in large but finite dimension. We show that our theory agrees with numerical simulations, state-of-the-art diffusion models trained on image data, as well as with lower diversity observed in practice (Sadat et al., 2023; Schwag et al., 2022).

**II.** Leveraging our theoretical analysis, we show that more general versions of CFG are possible, which enjoy the same properties as the standard linear CFG. We propose generalizations of CFG and experimentally demonstrate in the high-dimensional Gaussian mixture case their desirable properties, including smaller overshoot, dampened variance shrinkage and faster convergence to the target distribution. We apply non-linear CFG to class-conditional models (DiT Peebles and Xie (2023) and EDM2 Karras et al. (2024b)) trained on ImageNet-1K (Deng et al., 2009), as well as text-to-image models (MMDiT, Esser et al. (2024) and MDTv2, Gao et al. (2023)) trained on CC12M (Changpinyo et al., 2021), YFCC100M (Thomee et al., 2016) and a large internal dataset consisting of 320M Shutterstock images. Our findings show that non-linear CFG provides greater flexibility and improves generation quality.

## 2 Related Work

Classifier-Free Guidance (CFG) has been a topic of interest in recent research, with the original work introducing CFG (Ho and Salimans, 2022) highlighting the trade-off between image quality, measured by Fréchet inception distance (FID, Heusel et al. (2017)), and diversity, measured by inception score (Salimans et al., 2016) when adjusting the guidance strength parameter  $\omega$ . Since then, a significant body of research has examined CFG from various perspectives.

*Theoretical works on CFG.* From a theoretical standpoint, several works also employed Gaussian mixture models to analyze diffusion and guidance, including Chidambaram et al. (2024); Shah et al. (2023); Liang et al. (2024); Cui et al. (2023); Bai et al. (2024). In contrast, Du et al. (2023) explored alternative approaches to conditioning, modifying, and reusing diffusion models for compositional generation and guidance tasks. Bradley and Nakkiran (2024) characterized CFG as a predictor-corrector (Song et al., 2020a), positioning it within a broader context of sampling approaches in order to improve its theoretical understanding, similar to the approach in this paper, however from the perspective of denoising and sharpening processes.

*CFG variants and experimental analyses.* Among experimental evaluations of CFG, Karras et al. (2024a) showed that guiding generation using a smaller, less-trained version of the model itself can achieve disentangled control over image quality without compromising variation. Kynkäänniemi et al. (2024) proposed applying CFG in a limited interval, and Wang et al. (2024) proposed using weight schedulers for the classifier strength parameter. Several alternatives to standard CFG have been proposed, such as rectified classifier guidance (Xia et al., 2024) using pre-computed guidance coefficients, projected score guidance (Kadkhodaie et al., 2024) pushing the image feature vector toward a feature centroid of the target class, characteristic guidance (Zheng and Lan, 2023) as a non-linear correction of CFG obtained using numerical solvers, and second-order CFG (Sun et al., 2023) assuming locally-cone shaped condition space. All these variants can be directly combined with our proposed generalization of CFG.

*Dynamical regimes, statistical physics and high-dimensional settings.* Akin to this work, several works recently studied dynamical regimes of diffusion models, primarily focusing on the standard, non-CFG version (Biroli and Mézard, 2023; Raya and Ambrogioni, 2024; Biroli et al., 2024; Sclocchi et al., 2024; Yu and Huang, 2024; Li and Chen, 2024; Aranguri et al., 2025). Statistical physics methods have been particularly useful in analyzing high-dimensional settings, e.g., data drawn from the Curie-Weiss model (Biroli and Mézard, 2023), high-dimensional Gaussian mixtures (Biroli et al., 2024), and hierarchical models (Sclocchi et al., 2024). Other relevant statistical-physics studies include Ghio et al. (2024), who provided a comprehensive theoretical comparison between flow, diffusion, and autoregressive models from a spin glass perspective; Achilli et al. (2024), who extended the theory of memorization in generative diffusion to manifold-supported data; Cui et al. (2025, 2023), who analyzed sample complexity for high-dimensional Gaussian mixtures. A rigorous formulation of diffusion models in infinite dimensional setting was developed by Pidstrigach et al. (2023).

## 3 Background and High-Level Discussion

### 3.1 General Setup

We begin by providing an overview of the standard framework for generative diffusion, serving as the foundation for our analysis. We let  $\{\vec{a}_i\}_{i=1}^n \in \mathbb{R}^d$  represent  $n$  independent data points sampled from the *true* underlying data distribution  $P_0(\vec{a})$  that we aim to model.

The forward diffusion process, starting from the data points  $\{\vec{a}_i\}_{i=1}^n$ , is modeled by an Ornstein-Uhlenbeck process, described by the following stochastic differential equation:

$$d\vec{x}(t) = f(t)\vec{x}(t) dt + g(t) d\vec{B}(t), \quad (1)$$

where  $d\vec{B}(t)$  denotes the standard Wiener process (also known as Brownian motion) in  $\mathbb{R}^d$ . At any given time  $t$ , the state  $\vec{x}(t)$  is distributed according to a Gaussian distribution with mean  $s(t)\vec{a}$  and variance

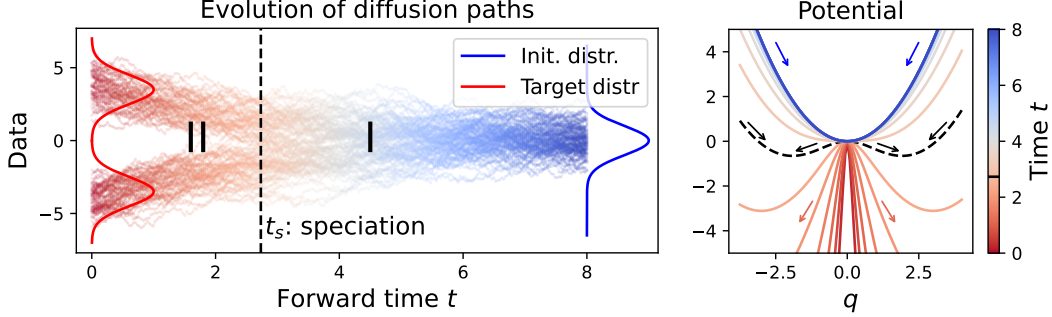


**Figure 2 Dynamical regimes in diffusion models.** **Left:** Illustration of the speciation phenomenon using a one-dimensional Gaussian mixture. Starting from pure Gaussian noise at large time  $t$ , the backward diffusion begins in Regime I, where the class has not been decided yet. After speciation time  $t_s$  (dashed line), the class membership is decided (speciation is a cross-over in  $d = 1$ , it becomes sharp for large  $d$ ). **Right:** time evolution of the effective potential for high-dimensional Gaussian mixture showcasing the symmetry breaking phenomenon.

$s(t)^2\sigma(t)^2$ , where  $s(t)$  and  $\sigma(t)$  are related to the functions  $f(t)$  and  $g(t)$  of Eq. (1) by  $s(t) = \exp \int_0^t d\tau f(\tau)$  and  $\sigma(t) = \int_0^t d\tau g(\tau)^2 / s(\tau)^2$ . The forward process is terminated at time  $t_f \gg 1$ , when  $\vec{x}(t_f)$  is effectively pure Gaussian noise, distributed as  $\mathcal{N}(0, s(t_f)^2\sigma(t_f)^2\mathcal{I}_d)$ , with  $\mathcal{I}_d$  being the identity matrix in  $\mathbb{R}^d$ . Note that for  $\{\vec{a}_i\}_{i=1}^n$  drawn from  $P_0$ , the distribution  $P_t(\vec{x})$  at time  $t$  is the convolution of the original distribution  $P_0$  with a Gaussian kernel.

The backward diffusion process operates in reverse time. Denoting reverse time variable by  $\tau = t_f - t$ , we can describe the process by the following stochastic equation:

$$d\vec{x}(\tau) = -f(\tau)\vec{x}d\tau + g(\tau)^2\vec{S}(\vec{x}, \tau)d\tau + g(\tau)d\vec{B}(\tau), \quad (2)$$

where  $\vec{S}(\vec{x}, \tau) = \vec{\nabla} \log P_\tau(\vec{x})$  denotes the score function. The backward diffusion process generates points  $\vec{x}$  sampled from the distribution  $P_t(\vec{x})$  for every time step  $\tau$ . At the end of the backward process, i.e., when  $\tau = t_f$ , the process generates points drawn from the original distribution  $P_0$ .

In this work, we focus on generating data that can be categorized into distinct classes. We begin by assuming that the underlying data distribution is a  $d$ -dimensional probability distribution  $P_0(\vec{x}, c)$ , where  $c$  represents a discrete class index and  $\vec{x}$  a  $d$ -dimensional vector. The aim is to generate data conditioned on  $c$ , the class label. The procedure that is mathematically guaranteed to generate the correct (conditioned) target distribution consists of using the true conditional score,  $\vec{S}_t(\vec{x}, c) = \vec{\nabla} \log P_t(\vec{x}|c)$  in Eq. (2). CFG, however, does not do that; it instead further directs diffusion in a manner proportional to the difference between conditional and unconditional scores:

$$S_t^{\text{CFG}}(\vec{x}, c) = (1 + \omega)S_t(\vec{x}, c) - \omega S_t(\vec{x}), \quad (3)$$

where  $\omega$  denotes the guidance strength parameter.

### 3.2 Classifier-Free Guidance Works in High Dimension

*CFG and distinct dynamical regimes.* Biroli and Mézard (2023) and Biroli et al. (2024) analyze the dynamical regimes of the backward generative process in Eq. (2) for the case of two classes as  $d \rightarrow \infty$  through the lens of statistical physics. They identify two distinct regimes<sup>1</sup> in the time-reversed process: in Regime I, the random dynamical trajectories have not yet committed to a particular class of data. In Regime II, the trajectories have committed to a class and generate the features necessary to produce samples from that class. This distinction is illustrated on a toy example in Figure 2. The transition between the two distinct dynamical regimes occurs at a crossover point called the *speciation time*, denoted  $t_s$ . Additionally, in cases with more

<sup>1</sup>Note that if the perfect empirical score is used, there exists a third regime, Regime III, characterized by *collapse*, i.e., memorization of the training set, but we shall not discuss it here as it is not relevant to CFG.

structured data with several classes and subclasses, multiple speciation times can exist, e.g., see [Li and Chen \(2024\)](#); [Sclocchi et al. \(2024\)](#). The emergence of these two dynamical regimes is related to a concentration phenomenon. In Regime II, the probability  $P_t(\vec{x})$  consists of separated non-overlapping lumps, related to the class to which the trajectories are heading.

We first provide a general explanation of CFG in this high-dimensional setting. In the next section, we present a detailed analysis for Gaussian mixtures. The unconditional score can be written in terms of the conditional scores as follows:

$$\vec{S}_t(\vec{x}) = \vec{\nabla} \log P_t(\vec{x}) = \frac{\sum_{c=1}^K P_t(\vec{x}|c)p(c) \vec{S}_t(\vec{x}, c)}{\sum_{c=1}^K P_t(\vec{x}|c)p(c)}, \quad (4)$$

where  $p(c)$  is the probability of class  $c$  in the original data (we assume the presence of  $K$  classes).

In high-dimensional settings, the speciation phenomenon ensures that once the backward process enters Regime II, any sample  $\vec{x}$  drawn from  $P_t(\vec{x})$  will almost surely belong to a single, well-defined class  $c$ . If  $\vec{x}$  is in the lump associated with class  $c$ , then  $\sum_{c'=1}^K P_t(\vec{x}|c')p(c') \rightarrow P_t(\vec{x}|c)p(c)$ . [Eq. \(4\)](#) then implies that the full score equals the one computed in the class  $c$ , *i.e.*,  $\vec{S}_t(\vec{x}, c) = \vec{S}_t(\vec{x})$ , and the additional guidance term introduced by CFG vanishes. Hence, CFG has no effect in Regime II. In contrast, during Regime I, before speciation occurs, CFG steers the dynamics toward the cluster  $c$  faster. However, this does not compromise the final sample quality, since the actual class-conditioned generation occurs in Regime II, where CFG no longer alters the distribution.

In conclusion, the existence of two regimes for high-dimensional data, Regime I in which the trajectory chooses the class, and Regime II in which the generation of the conditioned data takes place, offers a theoretical justification of the ability of CFG to reproduce the correct target distribution.

## 4 CFG in the High-Dimensional Limit of Gaussian Mixtures

Here, we demonstrate the applicability of the general argument presented in [Section 3](#) in a concrete case corresponding to high-dimensional Gaussian mixtures. We describe here the main findings, while the detailed analysis is provided in [App. B](#). Specifically, we examine the case in which  $P_0(\vec{a})$  represents a superposition of two Gaussians, each carrying equal weight, with means at  $\pm\vec{m}$  and shared isotropic variance  $\sigma^2$ . To ensure that the two Gaussian clusters remain well separated in the limit of high dimensionality, we take the large  $d$  limit with fixed values of  $|\vec{m}|^2/d$  and  $\sigma$ . We also assume that the score is correctly estimated. The extension to more than two Gaussian is straightforward and discussed in [App. E](#). To simplify the notation, we focus on the SDE forward equation corresponding to  $f(t) = -1$  and  $g(t) = \sqrt{2}$  (see [Eq. \(1\)](#)). All results can be easily translated for general choices of  $f(t), g(t)$ .

In this setting, the speciation transition resembles a symmetry-breaking phenomenon, similar to what occurs in thermodynamic phase transitions. [Biroli et al. \(2024\)](#) investigated this phenomenon by analyzing the backward dynamics and determined the speciation timescale as  $t_s = \frac{1}{2} \log(d)$ . In their analysis,  $t_s$  emerges as the timescale at which diffusion paths commit to a specific category. This is related to a change in the form of the potential in the backward Langevin equation, see [Figure 2](#) (right). Applying this framework we find that *the speciation time aligns precisely with the time until which CFG is effective* in aiding class selection. Beyond this point, as the trajectory has committed to a class, CFG no longer influences the generated outcome.

### 4.1 Deriving the CFG Score

The distribution of the points at time  $t$ ,  $P_t(\vec{x})$ , is the convolution of the initial distribution  $P_0$  and a diffusion kernel proportional to  $e^{-(\vec{x}-\vec{a}e^{-t})^2/(2\Delta_t)}$ :

$$P_t(\vec{x}) = \frac{1}{2\sqrt{2\pi}\Gamma_t^d} \left[ e^{-(\vec{x}-\vec{m}e^{-t})^2/(2\Gamma_t)} + e^{-(\vec{x}+\vec{m}e^{-t})^2/(2\Gamma_t)} \right],$$

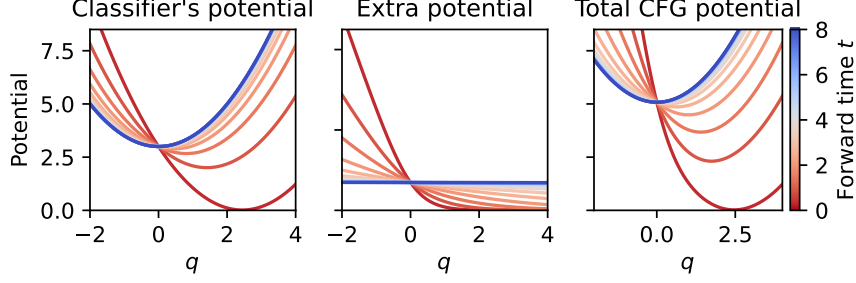


**Figure 3 Effect of CFG on the guiding potential of a Gaussian mixture.** The backward diffusion for the variable  $q$  giving the projection of  $\vec{x}$  on the center  $\vec{m}$  of the Gaussian where one wants to guide the backward diffusion. From left to right: Potential within the class, CFG-added-potential  $V_{\text{extra}}$  with  $\omega = 2$ , and their sum as in Eq. (7). CFG exhibits faster convergence to the target ( $t = 0$ ), but results in narrower potential for small  $t$  (with  $t$  ranging from 0 to 8, as indicated on the right panel).

where  $\Gamma_t = \sigma^2 e^{-2t} + \Delta_t = 1 + (\sigma^2 - 1)e^{-2t}$ , which approaches 1 as  $t$  becomes large. In this case, the classifier-free guidance formula in Eq. (3), with details given in App. A.2, can be rewritten as:

$$S_t^{\text{CFG}}(\vec{x}, c) = -\frac{\vec{x}}{\Gamma_t} + \frac{c\vec{m}e^t}{\Gamma_t} + \omega \frac{\vec{m}e^{-t}}{\Gamma_t} \left\{ c - \tanh\left(\frac{\vec{x} \cdot \vec{m}e^{-t}}{\Gamma_t}\right) \right\}, \quad (5)$$

with  $c = \pm 1$  and  $\omega > 0$ .

## 4.2 CFG Provides an Additional Push Toward the Desired Class in Regime I

We can analyze the score in Eq. (5) to identify which directions of the backward process are affected by CFG. Following Biroli et al. (2024), we first focus on Regime I, taking place on time-scales  $t_s + O(1) = (1/2) \log d + O(1)$ . Eq. (5) shows that the CFG-dependent part of the score is aligned on the  $\vec{m}$  direction, therefore CFG has no effect on the “transverse” directions  $\vec{v} \perp \vec{m}$ . The projection of the backward Eq. (2) on a unit vector in the space orthogonal to  $\vec{m}$  follows the equation  $dp = p(1 - 2/\Gamma_{t_f - \tau})d\tau + \sqrt{2}dB$ . This is the backward equation for an initial Gaussian  $\mathcal{N}(0, \sigma^2)$ , thus explicitly showing that all components of  $\vec{x}$  orthogonal to  $\vec{m}$  are unaffected by CFG and distributed as in the target distribution for  $\tau \rightarrow t_f$ .

However, when projecting onto  $\vec{m}$  we observe that the CFG score  $\vec{S}_t^{\text{CFG}}$  influences the component along  $\vec{m}$ . Defining  $q(t) := \frac{\vec{x} \cdot \vec{m}}{|\vec{m}|}$  where  $|\vec{m}| = \sqrt{d}$ , the evolution of the backward system in Eq. (2) guided to class  $c = 1$  is given by the following:

$$dq = \left( q + 2 \left[ -q + e^{-(t_f - t_s - \tau)} \left( (1 + \omega) - \omega \tanh\left( q e^{-(t_f - t_s - \tau)} \right) \right) \right] \right) d\tau + d\eta(\tau), \quad (6)$$

where again  $\tau = t_f - t$ , with  $t_s = (1/2) \log d$ ,  $\eta(\tau)$  is the square root of two times a Brownian motion, and we used the fact that in Regime I we have  $\Gamma_t \simeq 1$ . From now onward, we omit the dependency  $t(\tau)$  for backward time and simply use the notation  $t$  to avoid clutter and keep the notation simple.

Eq. (6) can be rewritten as:  $dq = -\frac{\partial V^{\text{CFG}}(q, \tau)}{\partial q} d\tau + d\eta(\tau)$ , where the effective potentials has two contributions:

$$V^{\text{CFG}} = \underbrace{\left( \frac{1}{2} q^2 - 2e^{-(t-t_s)} q \right)}_{\text{Classifier's potential}} + \omega \underbrace{\left[ -qe^{-(t-t_s)} + \ln \cosh\left( qe^{-(t-t_s)} \right) \right]}_{\text{Extra potential } V_{\text{extra}}}. \quad (7)$$

From Eq. (7), we observe that the effect of CFG is adding to the classifier potential an extra contribution, plotted in Figure 3. The extra potential adds an additional push toward the positive values of  $q$ , the ones corresponding to the class  $c = 1$ . As shown from the figure, the effect of CFG is particularly strong for

trajectories that deviate from the typical behavior and correspond to values of  $q$  associated to the wrong class (in the case  $c = 1$ , negative values of  $q$ ). For large  $\tau$ , when the dynamics is exiting Regime I, the value of  $qe^{-(t-t_s)}$  becomes very large and the extra potential vanishes, thus showing that the effect of CFG fades out.

The dynamical effect of CFG can be seen in Figure 4, where we simulate Eq. (6) for  $t_s = 1000, \sigma = 1$ , averaging over 10,000 trajectories. In agreement with the previous arguments, this figure shows that CFG pushes  $\bar{x}$  faster toward the desired class (higher values of  $q$  for  $c = 1$ ). Large  $\omega$  leads to an overshoot, but in the large  $d$  limit  $q$  then aligns with one of the classes when exiting Regime I, contrary to empirical observations made for  $d = 1$ , e.g., by Chidambaram et al. (2024), where the paths never realign.

### 4.3 CFG plays no role in Regime II

The variable  $q$  diverges at the end of Regime I and becomes of order  $\sqrt{d}$  in Regime II (as explained by Biroli et al. (2024)). One has therefore to focus on the rescaled variable  $\bar{x} \cdot \bar{m}/d$ . At the end of Regime I,  $q$  has realigned with the value it would have had for  $\omega = 0$ . Hence, the initial condition in Regime II (when guiding towards either of the classes,  $c = 1$  or  $c = -1$ ) is  $\bar{x} \cdot \bar{m}/d = 0$ , independently of  $\omega$ . Moreover, since in Regime II,  $|\bar{x} \cdot \bar{m}|e^{-t}/\Gamma_t$  is  $O(d)$  and  $\text{sign}(\bar{x} \cdot \bar{m}) = 1$ , one finds that the extra CFG term in Eq. (5) is zero since  $1 - \tanh(\bar{x} \cdot \bar{m}e^{-t}/\Gamma_t) \rightarrow 0$  for  $d \rightarrow \infty$ . Therefore, we are able to conclude that for  $t \ll t_s$ , for any  $\omega$ , in the large  $d$  limit the score obtained by CFG is equal to the score within the class  $S_t^{\text{CFG}}(\bar{x}, c) = S_t(\bar{x})$ , thus showing that CFG has no effect in Regime II.

Furthermore, using that at the time of exit from Regime I,  $q$  has the same value as for  $\omega = 0$ , the backward dynamics during Regime II leads to the correct conditioned target distribution at the end of the backward process for any  $\omega$ . This effect is shown in Figure 1 (right panel) in the case of  $d = 200$  and in Figure 4.

### 4.4 Finite Dimensional Effects: Overshoot of the Mean and Reduction of the Variance

So far, we have shown that for any value of  $\omega$  the target distribution is correctly reproduced in the infinite- $d$  limit. We now consider the changes brought by considering  $d$  large but finite. A detailed analysis is presented in App. C; here we present the main results.

The extra CFG term in the score, see Eq. (5), is of the same order as the one corresponding to the conditional score within Regime I and remains so, even for finite  $d$ . In contrast, in Regime II, the extra CFG term is zero for  $d \rightarrow \infty$  and exponentially small in  $d$  for finite  $d$ . Thus, for large but finite dimensions, results obtained for  $d \rightarrow \infty$  carry over: CFG has a substantial effect only in Regime I and, hence, only on the initial condition for the dynamics in Regime II.

The effect of CFG in Regime I is to add an extra push toward the desired class. Indeed, the sign of the term introduced by CFG in the score accords with the desired class: in the Langevin equation it gives an extra contribution to the force which is positive for  $c = +1$ , and negative for  $c = -1$ . In consequence, the generated distribution shows an overshoot corresponding to the target distribution since its mean is larger for  $c = +1$ , smaller for  $c = -1$ . The relative amplitude of the overshoot for Regime II is of order  $1/\sqrt{d}$ , and it is due to the role of CFG on the dynamics of Regime I. The extra term due to CFG has another important effect: it leads to a larger second derivative of the potential  $V^{\text{CFG}}(q, t)$ , see Figure 3 and App. C. Thus, the resulting CFG Langevin equation is associated to a potential that is more confining. This explains the numerical observation where we find that the CFG-generated distribution has a smaller variance than the one of the target distribution. The mean overshoot and the decrease in the variance for different guidance strengths are shown in Figure 10 in App. C.

Two main conclusions result from this analysis. First, the error due to CFG for finite  $d$  agrees well with

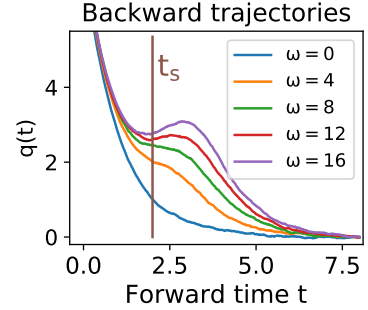


**Figure 4** Evolution of the mean of  $q(t)$ . It starts from 0 at large forward time  $t$ , and is pushed towards positive values (cluster centered in  $+\bar{m}$ ) when  $t$  decreases. It can be observed that CFG is effective when  $t \gtrsim t_s$  (vertical line) and stronger for larger values of  $\omega$ . In Regime II, the trajectories of  $q$  for various values of  $\omega$  merge.

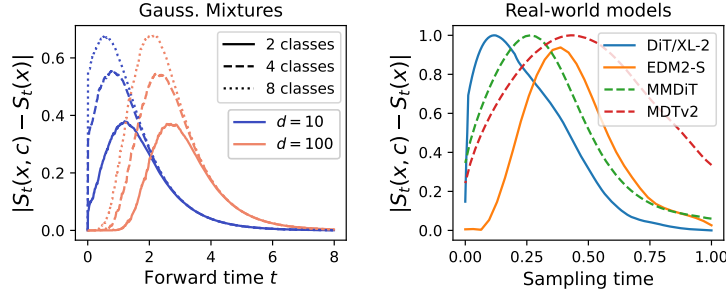


**Figure 5 Left:** Numerically simulating mixture of two, four, and eight Gaussians with equidistant means on a sphere ( $r = \sqrt{d}$ ), with varying dimension  $d$ , with  $\omega = 4, \sigma^2 = 1$ , averaged over 10,000 trajectories. As  $d$  increases, the score difference is substantial on earlier backward times  $\tau$  (in Regime I). Additionally, as the number of classes increases, the magnitude of the score difference grows, as well as the duration of large difference between the scores. **Right:** We replicated the same experiment using class-conditional (DiT/XL-2 and EDM2-S) and text-to-image (MMDiT and MDTv2) diffusion models. For presentation clarity, we normalized x-axis timesteps and y-axis score difference to range  $[0, 1]$ . We observed a consistent pattern with theory: monotonically increasing score difference followed by decay after a certain point.

what was found in numerical experiments and in analysis of very low dimensional cases (Wu et al., 2024; Chidambaram et al., 2024; Xia et al., 2024; Bradley and Nakkiran, 2024). Second, since CFG has no role in Regime II, as was implicitly observed by Kynkäänniemi et al. (2024)<sup>2</sup>, and causes an overshoot when it is kept too long in Regime I, it would be desirable to switch it off before  $t_s$ , as shown for high-dimensional Gaussian mixtures in Figure 9 in App. C. In the following section, we propose a generalization of CFG that automatically switches off in Regime II, showing in practice it can yield better quality, higher diversity and faster convergence to the target distribution, while being less computationally expensive.

## 5 More General Guidance Forms

### 5.1 Non-Linear Classifier-Free Guidance

The blessing of dimensionality that makes CFG work in high-dimensions is due to two main properties: (1) CFG acts in Regime I pushing further in the direction of the desired class, (2) CFG does not play any role in Regime II where the detailed property of the data are generated.

This observation makes clear that CFG can be generalized to encompass other guidance schemes that still enjoy the two properties cited above. With this idea in mind, we propose non-linear variants of the CFG score of the type:

$$S_t^{\text{CFG-NL}}(\vec{x}, c) = S_t(\vec{x}, c) + [S_t(\vec{x}, c) - S_t(\vec{x})] \phi_t \left( \left| \vec{S}_t(\vec{x}, c) - \vec{S}_t(\vec{x}) \right| \right). \quad (8)$$

For constant  $\phi_t(s) = \omega$ , this reduces to standard CFG. As long as the function  $\phi_t(s)$  satisfies  $\lim_{s \rightarrow 0} [s\phi_t(s)] = 0$ , we know that in Regime II the extra contribution to the score due to  $\phi_t$  vanishes, thus leading to a correct target distribution in high-dimension. The freedom in the choice of  $\phi_t$  can be used to improve the effect of CFG in Regime I, helping to push the system in the direction of class  $c$ , and reducing the unwanted finite dimensional drawbacks leading to mean overshoot and reduced variance. In the following, as a proof of principle, we propose a first candidate for  $\phi_t$ . As we shall show, this choice already allows to improve very efficient generative models. In the long run, we envisage that the whole function  $\phi_t$  can be optimized as hyper-parameters.

<sup>2</sup>Kynkäänniemi et al. (2024) observe in Fig. 5 (right) of their paper that stopping guidance after noise level  $\sigma_{low} \approx 0.85$  has no effect on image quality, measured by Fréchet inception distance.

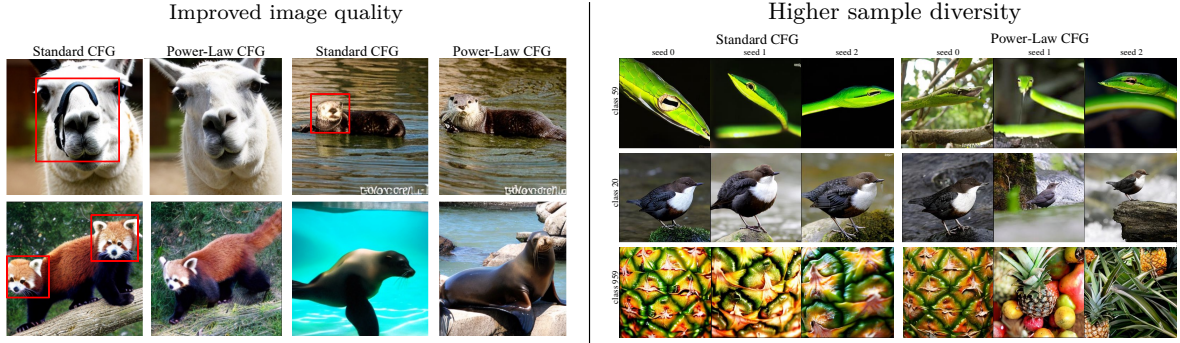


**Figure 6** Qualitative comparison between Standard CFG ( $\omega = 4$ ) and Power-Law CFG ( $\omega = 4, \alpha = 0.1$ ) on DiT/XL-2 trained on ImageNet-1K at  $256 \times 256$  resolution. **Left panel:** Each paired image starts from same initial noise with standard (left) and Power-Law CFG (right). Power-Law often exhibits improved details which might contribute to the improved FID. **Right panel:** For three classes, starting from same seeds (0, 1 and 2), Power-Law CFG generates images with higher diversity. Further qualitative examples are provided in App. H.

## 5.2 Power-Law CFG

We can choose  $\phi_t(s) = \omega s^{-\alpha}$  with  $\alpha < 1$  to obtain the following guidance scheme:

$$\vec{S}_t^{\text{PL}}(\vec{x}, c) = S_t(\vec{x}, c) + \omega [S_t(\vec{x}, c) - S_t(\vec{x})] \left| \vec{S}_t(\vec{x}, c) - \vec{S}_t(\vec{x}) \right|^{-\alpha}.$$

One can understand the effect of this non-linear guidance as follows. The  $\ell_2$  distance between scores  $\delta S = |\vec{S}_t(\vec{x}, c) - \vec{S}_t(\vec{x})|$  vanishes as  $e^{-t}$  at large (forward) times, as all the forward trajectories starting from an initial point  $\vec{a}$  build at time  $t$  a Gaussian cloud. Therefore w.r.t. the standard CFG in Eq. (3), this new score acts with an effective guidance strength which changes  $\omega$  to  $\omega[\delta S]^{-\alpha}$ , making it stronger at the beginning of the backward process. Then, when the backward process gets closer to the speciation time,  $\delta S$  decreases, the non-linear strength becomes weaker, and it vanishes in Regime II<sup>3</sup>, as displayed in Figure 8 in App. A.

*Additional Non-Linear CFG forms.* Another valid choice is  $\phi_t(s) = \omega \cdot \mathbb{I}_{[t_1, t_2)}(t)$  where  $\mathbb{I}$  denotes the indicator function, applying CFG only at  $t \in [t_1, t_2)$ , as examined by Kynkäänniemi et al. (2024) and detailed in App. G. The authors perform a grid search for hyperparameters  $t_1$  and  $t_2$ , but this can be costly. Instead, we propose a heuristic that performs almost nearly as well: estimating  $t_1$  as the first backward time when  $\phi_t(s)$  exceeds its mean, and  $t_2$  as the timestep of the mode of  $\phi_t(s)$ , estimated through a few warm-up sampling runs. Another effective choice for  $\phi_t(s) = \omega_t$  relies only on weight schedulers for the guidance parameter (disregarding the score difference), as examined by Wang et al. (2024).

We emphasize that the non-linear CFG and the rest of our framework, although introduced for backward SDEs, can be applied to Flow Matching (Lipman et al., 2022) and Stochastic Interpolants (Albergo et al., 2023).

## 5.3 Generative image model experiments

*Models, architectures and datasets.* We validate our theoretical findings and test the performance of non-linear CFG both through numerical simulations with Gaussian mixtures with varying dimensions and number of classes, and five generative image models. The latter include: DiT (Peebles and Xie, 2023) as a standard diffusion framework and EDM2 (Karras et al., 2024b) as a state-of-the-art one. We test DiT-XL/2 and EDM2-S versions, trained and evaluated on ImageNet-1k (resolution 256 and 512 respectively) for class conditional generation. We also consider three text-to-image models. The first two models are trained on ImageNet-1k and CC12M (Changpinyo et al., 2021) and evaluated on CC12M, using the diffusion DDPM training objective (Ho et al., 2020) with MMDiT (Esser et al. (2024), similar to SD3) and MDTv2 (Gao et al., 2023) architectures scaled to 800M parameters. The last model uses a MMDiT architecture scaled to 1.6B parameters and is trained with a flow matching objective on YFCC100M (Thomee et al., 2016), CC12M and

<sup>3</sup>For computational reasons, one could stop applying guidance once the score difference becomes sufficiently small.

**Table 1 Quantitative results.** Image quality (FID, top block) and sample diversity (Recall, bottom block) across several model architectures and datasets. Compared to Standard CFG and the powered cosine schedule (first and second row respectively), Power-Law CFG (*NL-Stand.*) improves both metrics. When combined with limited guidance scheme using the proposed heuristic (*NL-Lim.v2*), performance further improves. Column *#p.* indicates the number of hyperparameters, ‘-FM’ denotes flow matching training objective, an asterisk ‘\*’ denotes full guidance outperformed limited interval performance. Experimental details are provided in App. D.

Metric	Type	#p.	DiT/XL-2 <i>IM256</i>	EDM2-S <i>IM512</i>	MMDiT <i>CC12M</i>	MDTv2 <i>CC12M</i>	MMDiT-FM <i>COCO</i>
FID (↓)	Standard	1	2.24	2.23	8.6	8.5	5.2
	Scheduler	2	2.14	1.95	<b>8.3</b>	8.2	5.0
	NL-Stand.	2	<b>2.09</b>	<b>1.86</b>	<b>8.3</b>	<b>8.1</b>	<b>4.9</b>
	Limited	3	<b>1.97</b>	1.69	8.58	<b>8.5*</b>	<b>5.0</b>
	Lim. v2	1	2.01	1.7	8.65	8.8	5.1
	NL-Lim.v2	2	2.00	<b>1.67</b>	<b>8.57</b>	8.6	<b>5.0</b>
Recall (↑)	Standard	1	0.575	0.582	0.562	0.522	0.594
	Scheduler	2	<b>0.599</b>	0.591	0.559	0.534	0.606
	NL-Stand.	2	0.596	<b>0.600</b>	<b>0.565</b>	<b>0.537</b>	<b>0.613</b>
	Limited	3	0.602	0.598	<b>0.553</b>	0.527	0.608
	Lim. v2	1	0.600	0.602	0.549	0.524	0.601
	NL-Lim.v2	2	<b>0.614</b>	<b>0.612</b>	0.552	<b>0.531</b>	<b>0.615</b>

a proprietary dataset of 320M Shutterstock images, evaluated on COCO dataset (Lin et al., 2014). To ensure the protection of personal data, we blurred human faces in ImageNet-1K and CC12M. Additionally, we utilized Florence-2 (Xiao et al., 2023) to recaption images resulting in more accurate image content descriptions.

*Comparing numerical simulations of a mixture of Gaussians to real-world experiments.* In Figure 5 we observe similar hump-shaped behavior of the difference between conditional and unconditional score  $|S_t(\vec{x}, c) - S_t(\vec{x})|$  for Gaussian mixtures and that of real-world models, both for class-conditional and text-to-image models, thus validating one of the main points of our theoretical framework. Using the parameter  $\alpha$  in Power-law CFG, we can alter the shape of these curves, therefore obtaining more flexible frameworks generalizing standard CFG (see Figure 8 in App. B). We find that this flexibility enables faster convergence, yielding paths that consistently have smaller Jensen-Shannon divergence to the target distribution (across all time  $\tau$ ), reaching the target distribution faster as well as reducing the overshoot of the target distribution (see Fig. 14, App. E).

*Improving image quality and diversity by non-linear CFG.* To evaluate our method, we employed FID (Heusel et al., 2017) measuring image quality, and recall (Sajjadi et al., 2018) measuring diversity. Exact experimental configurations can be found in App. D.2. We benchmarked against the best-performing weight scheduler heuristic from Wang et al. (2024), the dynamic powered-cosine  $\omega_t = 0.5(1 - \cos \pi(1 - t/T)^s)\omega$ , with  $s, \omega$  tunable parameters and  $T$  the number of denoising steps. As shown in Table 1, Power-Law CFG performs favorably both in terms of FID and recall. Furthermore, our proposed step-wise CFG heuristic achieved comparable performance to performing hyperparameter search over  $t_1$  and  $t_2$  but with two fewer hyperparameters, while further combining it with Power-Law yielded slight improvement in FID and notable improvement in recall. Qualitative examples are provided in Figure 6, with additional examples included in App. H (class-conditional) and App. I (text-to-image), displaying the improved realism and the increased diversity of the generated images.

While Power-Law CFG demonstrates consistent benefits across different training objectives, noise schedulers, sampling methods, network architectures and datasets, its performance relative to other possible non-linear guidance strategies remains unexplored. We believe there may be more effective and advantageous strategies, which are worth exploring in future work.

## 6 Conclusion

We studied the theoretical foundations of classifier-free guidance (CFG), a widely used method with practical benefits but limited theoretical understanding. Our research revealed that CFG’s inaccuracies in low-dimensional spaces do not hold true in the high-dimensional limit, yielding a "blessing-of-dimensionality" result. We extended our conclusions to large but finite dimensions, characterizing the discrepancies in lower dimensions. Building on our theoretical analysis, we developed a generalized version of CFG and confirmed its effectiveness through both numerical and real-world experiments, applying it successfully to leading efficient diffusion models. Our results demonstrated improved sample quality and diversity, while reducing the required computation. Future research directions could include a comprehensive evaluation of the advantages and limitations of non-linear CFG in comparison to alternative guidance methods, as well as designing new non-linear CFG techniques.

## Impact Statement

This study contributes to the growing body of research aimed at deepening our theoretical understanding of diffusion models and their broader implications for generative modeling. By bridging the gap between theory and practice, we strive to improve the performance and efficiency of these models, which have far-reaching applications in various fields.

However, as with any powerful technology, there are also potential risks associated with the development and deployment of advanced generative models. The increasing sophistication of deepfakes, for instance, raises concerns about misinformation, propaganda, and the erosion of trust in digital media. Moreover, the misuse of generative models for malicious purposes, such as creating fake identities or spreading disinformation, poses significant threats to individuals, communities, and society as a whole.

In light of these challenges, we hope that our paper, along with many others that aim to ameliorate understanding of these models, will contribute to a deeper understanding of their strengths and limitations. We believe that this is essential for developing effective strategies to mitigate the risks associated with generative models, and we hope that our work will be a step toward achieving this goal.

## Acknowledgements

This work has received funding from the French government, managed by the National Research Agency (ANR), under the France 2030 program with the reference ANR-23-IACL-0008. Furthermore, this paper is supported by PNR-PE-AI FAIR project funded by the NextGeneration EU program. We would like to thank Mathurin Videau, João Maria Janeiro, Kunhao Zheng, Tariq Berrada Ifriqi, Wes Bouaziz and Tony Bonnaire for fruitful discussions regarding the numerical experiments. We would further like to thank Levent Sagun, David Lopez-Paz, Brian Karrer, Yaron Lipman and Luke Zettlemoyer for feedback and support. Finally, we also thank Carolyn Krol and Carolina Braga for extensive consultation and support throughout this project.

## References

- Beatrice Achilli, Enrico Ventura, Gianluigi Silvestri, Bao Pham, Gabriel Raya, Dmitry Krotov, Carlo Lucibello, and Luca Ambrogioni. Losing dimensions: Geometric memorization in generative diffusion. *arXiv preprint arXiv:2410.08727*, 2024.
- Michael S Albergo, Nicholas M Boffi, and Eric Vanden-Eijnden. Stochastic interpolants: A unifying framework for flows and diffusions. *arXiv preprint arXiv:2303.08797*, 2023.
- Santiago Aranguri, Giulio Biroli, Marc Mezard, and Eric Vanden-Eijnden. Optimizing noise schedules of generative models in high dimensions. *arXiv preprint arXiv:2501.00988*, 2025.
- Weimin Bai, Yifei Wang, Wenzheng Chen, and He Sun. An expectation-maximization algorithm for training clean diffusion models from corrupted observations. *arXiv preprint arXiv:2407.01014*, 2024.
- James Betker, Gabriel Goh, Li Jing, Tim Brooks, Jianfeng Wang, Linjie Li, Long Ouyang, Juntang Zhuang, Joyce Lee, Yufei Guo, et al. Improving image generation with better captions. *Computer Science*. <https://cdn.openai.com/papers/dall-e-3.pdf>, 2(3):8, 2023.
- Giulio Biroli and Marc Mézard. Generative diffusion in very large dimensions. *Journal of Statistical Mechanics: Theory and Experiment*, 2023(9):093402, 2023.
- Giulio Biroli, Tony Bonnaire, Valentin De Bortoli, and Marc Mézard. Dynamical regimes of diffusion models. *arXiv preprint arXiv:2402.18491*, 2024.
- Arwen Bradley and Preetum Nakkiran. Classifier-free guidance is a predictor-corrector. *arXiv preprint arXiv:2408.09000*, 2024.
- Soravit Changpinyo, Piyush Sharma, Nan Ding, and Radu Soricut. Conceptual 12m: Pushing web-scale image-text pre-training to recognize long-tail visual concepts. In *Proceedings of the IEEE/CVF conference on computer vision and pattern recognition*, pages 3558–3568, 2021.
- Muthu Chidambaram, Khashayar Gatmiry, Sitan Chen, Holden Lee, and Jianfeng Lu. What does guidance do? a fine-grained analysis in a simple setting. *arXiv Preprint*, 2409.13074, 2024.
- Hugo Cui, Florent Krzakala, Eric Vanden-Eijnden, and Lenka Zdeborová. Analysis of learning a flow-based generative model from limited sample complexity. *arXiv preprint arXiv:2310.03575*, 2023.
- Hugo Cui, Cengiz Pehlevan, and Yue M Lu. A precise asymptotic analysis of learning diffusion models: theory and insights. *arXiv preprint arXiv:2501.03937*, 2025.
- Xiaoliang Dai, Ji Hou, Chih-Yao Ma, Sam Tsai, Jialiang Wang, Rui Wang, Peizhao Zhang, Simon Vandenhende, Xiaofang Wang, Abhimanyu Dubey, Matthew Yu, Abhishek Kadian, Filip Radenovic, Dhruv Mahajan, Kungpeng Li, Yue Zhao, Vladan Petrovic, Mitesh Kumar Singh, Simran Motwani, Yi Wen, Yiwen Song, Roshan Sumbaly, Vignesh Ramanathan, Zijian He, Peter Vajda, and Devi Parikh. Emu: Enhancing image generation models using photogenic needles in a haystack. *arXiv Preprint*, 2309.15807, 2023.
- Jia Deng, Wei Dong, Richard Socher, Li-Jia Li, Kai Li, and Li Fei-Fei. Imagenet: A large-scale hierarchical image database. In *2009 IEEE conference on computer vision and pattern recognition*, pages 248–255. Ieee, 2009.
- Prafulla Dhariwal and Alexander Nichol. Diffusion models beat gans on image synthesis. In *Advances in neural information processing systems*, 2021.
- Yilun Du, Conor Durkan, Robin Strudel, Joshua B Tenenbaum, Sander Dieleman, Rob Fergus, Jascha Sohl-Dickstein, Arnaud Doucet, and Will Sussman Grathwohl. Reduce, reuse, recycle: Compositional generation with energy-based diffusion models and mcmc. In *International conference on machine learning*, pages 8489–8510. PMLR, 2023.
- Patrick Esser, Sumith Kulal, Andreas Blattmann, Rahim Entezari, Jonas Müller, Harry Saini, Yam Levi, Dominik Lorenz, Axel Sauer, Frederic Boesel, et al. Scaling rectified flow transformers for high-resolution image synthesis. In *Forty-first International Conference on Machine Learning*, 2024.
- Shanghua Gao, Pan Zhou, Ming-Ming Cheng, and Shuicheng Yan. Masked diffusion transformer is a strong image synthesizer. In *Proceedings of the IEEE/CVF International Conference on Computer Vision*, pages 23164–23173, 2023.

- Davide Ghio, Yatin Dandi, Florent Krzakala, and Lenka Zdeborová. Sampling with flows, diffusion, and autoregressive neural networks from a spin-glass perspective. *Proceedings of the National Academy of Sciences*, 121(27):e2311810121, 2024.
- Melissa Hall, Oscar Mañas, Reyhane Askari, Mark Ibrahim, Candace Ross, Pietro Astolfi, Tariq Berrada Ifriqi, Marton Havasi, Yohann Benchetrit, Karen Ullrich, et al. Evalgim: A library for evaluating generative image models. *arXiv preprint arXiv:2412.10604*, 2024.
- Martin Heusel, Hubert Ramsauer, Thomas Unterthiner, Bernhard Nessler, and Sepp Hochreiter. Gans trained by a two time-scale update rule converge to a local nash equilibrium. *Advances in neural information processing systems*, 30, 2017.
- Jonathan Ho and Tim Salimans. Classifier-free diffusion guidance. *arXiv preprint arXiv:2207.12598*, 2022.
- Jonathan Ho, Ajay Jain, and Pieter Abbeel. Denoising diffusion probabilistic models, 2020. <https://arxiv.org/abs/2006.11239>.
- Zahra Kadkhodaie, Stéphane Mallat, and Eero P Simoncelli. Feature-guided score diffusion for sampling conditional densities. *arXiv preprint arXiv:2410.11646*, 2024.
- Tero Karras, Miika Aittala, Timo Aila, and Samuli Laine. Elucidating the design space of diffusion-based generative models. *Advances in neural information processing systems*, 35:26565–26577, 2022.
- Tero Karras, Miika Aittala, Tuomas Kynkäänniemi, Jaakko Lehtinen, Timo Aila, and Samuli Laine. Guiding a diffusion model with a bad version of itself. *arXiv preprint arXiv:2406.02507*, 2024a.
- Tero Karras, Miika Aittala, Jaakko Lehtinen, Janne Hellsten, Timo Aila, and Samuli Laine. Analyzing and improving the training dynamics of diffusion models. In *Proceedings of the IEEE/CVF Conference on Computer Vision and Pattern Recognition*, pages 24174–24184, 2024b.
- Tuomas Kynkäänniemi, Miika Aittala, Tero Karras, Samuli Laine, Timo Aila, and Jaakko Lehtinen. Applying guidance in a limited interval improves sample and distribution quality in diffusion models. *arXiv preprint arXiv:2404.07724*, 2024.
- Marvin Li and Sitan Chen. Critical windows: non-asymptotic theory for feature emergence in diffusion models. *arXiv preprint arXiv:2403.01633*, 2024.
- Yingyu Liang, Zhenmei Shi, Zhao Song, and Yufa Zhou. Unraveling the smoothness properties of diffusion models: A gaussian mixture perspective. *arXiv preprint arXiv:2405.16418*, 2024.
- Tsung-Yi Lin, Michael Maire, Serge Belongie, James Hays, Pietro Perona, Deva Ramanan, Piotr Dollár, and C Lawrence Zitnick. Microsoft coco: Common objects in context. In *Computer Vision—ECCV 2014: 13th European Conference, Zurich, Switzerland, September 6–12, 2014, Proceedings, Part V 13*, pages 740–755. Springer, 2014.
- Yaron Lipman, Ricky TQ Chen, Heli Ben-Hamu, Maximilian Nickel, and Matt Le. Flow matching for generative modeling. *arXiv preprint arXiv:2210.02747*, 2022.
- Alex Nichol, Prafulla Dhariwal, Aditya Ramesh, Pranav Shyam, Pamela Mishkin, Bob McGrew, Ilya Sutskever, and Mark Chen. Glide: Towards photorealistic image generation and editing with text-guided diffusion models. *arXiv preprint arXiv:2112.10741*, 2021.
- William Peebles and Saining Xie. Scalable diffusion models with transformers. In *Proceedings of the IEEE/CVF International Conference on Computer Vision*, pages 4195–4205, 2023.
- Jakiw Pidstrigach, Youssef Marzouk, Sebastian Reich, and Sven Wang. Infinite-dimensional diffusion models, 2023. <https://arxiv.org/abs/2302.10130>.
- Gabriel Raya and Luca Ambrogioni. Spontaneous symmetry breaking in generative diffusion models. *Advances in Neural Information Processing Systems*, 36, 2024.
- Seyedmorteza Sadat, Jakob Buhmann, Derek Bradley, Otmar Hilliges, and Romann M Weber. Cads: Unleashing the diversity of diffusion models through condition-annealed sampling. *arXiv preprint arXiv:2310.17347*, 2023.
- Chitwan Saharia, William Chan, Saurabh Saxena, Lala Li, Jay Whang, Emily L Denton, Kamyar Ghasemipour, Raphael Gontijo Lopes, Burcu Karagol Ayan, Tim Salimans, et al. Photorealistic text-to-image diffusion models with deep language understanding. *Advances in neural information processing systems*, 35:36479–36494, 2022.
- Mehdi SM Sajjadi, Olivier Bachem, Mario Lucic, Olivier Bousquet, and Sylvain Gelly. Assessing generative models via precision and recall. *Advances in neural information processing systems*, 31, 2018.

- Tim Salimans, Ian Goodfellow, Wojciech Zaremba, Vicki Cheung, Alec Radford, and Xi Chen. Improved techniques for training gans. *Advances in neural information processing systems*, 29, 2016.
- Antonio Sclocchi, Alessandro Favero, and Matthieu Wyart. A phase transition in diffusion models reveals the hierarchical nature of data. *arXiv preprint arXiv:2402.16991*, 2024.
- Vikash Sehwal, Caner Hazirbas, Albert Gordo, Firat Ozgenel, and Cristian Canton. Generating high fidelity data from low-density regions using diffusion models. In *Proceedings of the IEEE/CVF Conference on Computer Vision and Pattern Recognition*, pages 11492–11501, 2022.
- Kulin Shah, Sitan Chen, and Adam Klivans. Learning mixtures of gaussians using the ddpmm objective. *Advances in Neural Information Processing Systems*, 36:19636–19649, 2023.
- Jascha Sohl-Dickstein, Eric A. Weiss, Niru Maheswaranathan, and Surya Ganguli. Deep unsupervised learning using nonequilibrium thermodynamics, 2015. <https://arxiv.org/abs/1503.03585>.
- Yang Song and Stefano Ermon. Generative modeling by estimating gradients of the data distribution, 2020. <https://arxiv.org/abs/1907.05600>.
- Yang Song, Jascha Sohl-Dickstein, Diederik P Kingma, Abhishek Kumar, Stefano Ermon, and Ben Poole. Score-based generative modeling through stochastic differential equations. *arXiv preprint arXiv:2011.13456*, 2020a.
- Shikun Sun, Longhui Wei, Zhicai Wang, Zixuan Wang, Junliang Xing, Jia Jia, and Qi Tian. Inner classifier-free guidance and its taylor expansion for diffusion models. In *The Twelfth International Conference on Learning Representations*, 2023.
- Bart Thomee, David A Shamma, Gerald Friedland, Benjamin Elizalde, Karl Ni, Douglas Poland, Damian Borth, and Li-Jia Li. Yfcc100m: The new data in multimedia research. *Communications of the ACM*, 59(2):64–73, 2016.
- Qing Wang, Sanjeev R Kulkarni, and Sergio Verdú. Divergence estimation for multidimensional densities via  $k$ -nearest-neighbor distances. *IEEE Transactions on Information Theory*, 55(5):2392–2405, 2009.
- Xi Wang, Nicolas Dufour, Nefeli Andreou, Marie-Paule Cani, Victoria Fernández Abrevaya, David Picard, and Vicky Kalogeiton. Analysis of classifier-free guidance weight schedulers. *arXiv Preprint*, 2404.13040, 2024.
- Yuchen Wu, Minshuo Chen, Zihao Li, Mengdi Wang, and Yuting Wei. Theoretical insights for diffusion guidance: A case study for gaussian mixture models. *arXiv preprint arXiv:2403.01639*, 2024.
- Mengfei Xia, Nan Xue, Yujun Shen, Ran Yi, Tieliang Gong, and Yong-Jin Liu. Rectified diffusion guidance for conditional generation. *arXiv preprint arXiv:2410.18737*, 2024.
- Bin Xiao, Haiping Wu, Weijian Xu, Xiyang Dai, Houdong Hu, Yumao Lu, Michael Zeng, Ce Liu, and Lu Yuan. Florence-2: Advancing a unified representation for a variety of vision tasks (2023). URL <https://arxiv.org/abs/2311.06242>, 2023.
- Zhendong Yu and Haiping Huang. Nonequilibrium physics of generative diffusion models. *arXiv preprint arXiv:2405.11932*, 2024.
- Candi Zheng and Yuan Lan. Characteristic guidance: Non-linear correction for ddpmm at large guidance scale. *arXiv preprint arXiv:2312.07586*, 2023.
- Jean Zinn-Justin. *Quantum field theory and critical phenomena*, volume 171. Oxford university press, 2021.

# Appendix

The supplementary material is structured as follows:

- In Section A, we give a brief introduction of related work, mainly focusing on the work by [Biroli et al. \(2024\)](#).
- In Section B, we present experimental details for numerical simulations involving Gaussian Mixtures.
- In Section C, we present the theoretical and numerical findings for finite dimension (including low dimension  $d$ ).
- In Section D we provide experimental details involving real-world experiments.
- In Section E, we give the calculation required for computing the CFG score of a mixture of four Gaussians.
- In Section F, we perform further numerical experiments examining the non-linear CFG forms.
- In Section G, we draw a parallel to the work of [Kynkäänniemi et al. \(2024\)](#), showing that the time interval at which the guidance is applied aligns with our findings.

## A Introduction to related work: Classifier-free Guidance (CFG) and Specification Time in the High-Dimensional Limit

We start by briefly introducing the calculation required for estimating the speciation time  $t_s$  for a case of two equally weighted Gaussians. This section is a direct adaptation of the framework introduced by [Biroli et al. \(2024\)](#). The diffusion process, consisting of  $d$  independent Ornstein-Uhlenbeck Langevin equations, reads as follows (using  $f(t) = -1$  and  $g(t) = \sqrt{2}$  in [Eq. \(1\)](#)):

$$d\vec{x}(t) = -\vec{x}dt + d\vec{B}(t), \quad (9)$$

where  $d\vec{B}(t)$  equals the square root of two times the standard Brownian motion in  $\mathbb{R}^d$ . At time  $t = 0$ , the process starts from the probability distribution  $P_0(\vec{a})$ , consisting of two Gaussian clusters that have means at  $\pm\vec{m}$  and share the same variance  $\sigma^2$ . To guarantee that these Gaussians remain distinct in high-dimensional space, we assume that  $|\vec{m}|^2 = d\tilde{\mu}^2$ , where both  $\sigma$  and  $\tilde{\mu}$  are of order 1.

As the process evolves, the emergence of speciation resembles symmetry breaking observed during thermodynamic phase transitions. A common approach to analyzing this phenomenon is to construct a perturbative expansion of the free energy as a function of the field. Therefore, [Biroli et al. \(2024\)](#) derive an expression for  $\log P_t(\vec{x})$  using a perturbative expansion in terms of  $e^{-t}$ , which is valid for large time values. This method is justified since speciation occurs at large times.

One can rewrite the probability to be at  $\vec{x}$  at time  $t$  as

$$\begin{aligned} P_t(\vec{x}) &= \int d\vec{a} P_0(\vec{a}) \frac{1}{\sqrt{2\pi\Delta_t^d}} \exp\left(-\frac{1}{2} \frac{(\vec{x} - \vec{a}e^{-t})^2}{\Delta_t}\right) \\ &= \frac{1}{\sqrt{2\pi\Delta_t}} \exp\left(-\frac{1}{2} \frac{\vec{x}^2}{\Delta_t} + g(\vec{x})\right), \end{aligned}$$

where the function  $g(\vec{x})$ , defined as

$$g(\vec{x}) = \log \int d\vec{a} P_0(\vec{a}) \exp\left(-\frac{1}{2} \frac{\vec{a}^2 e^{-2t}}{\Delta_t}\right) \exp\left(\frac{e^{-t}\vec{x} \cdot \vec{a}}{\Delta_t}\right)$$

can be viewed through a field-theoretic (or equivalently, a probabilistic) approach, where it serves as a generative function for connected correlations among the variables  $\vec{a}$  (Zinn-Justin, 2021). By expanding this function at large times, one can show:

$$g(\vec{x}) = \frac{e^{-t}}{\Delta_t} \sum_{i=1}^d x_i \langle a_i \rangle + \frac{1}{2} \frac{e^{-2t}}{\Delta_t^2} \sum_{i,j=1}^d x_i x_j \left[ \langle a_i a_j \rangle - \langle a_i \rangle \langle a_j \rangle \right] + O\left((xe^{-t})^3\right),$$

where we utilize the brackets  $\langle \cdot \rangle$  to denote the expectation value with respect to the effective distribution  $P_0(\vec{a})e^{-\vec{a}^2 e^{-2t}/(2\Delta_t)}$ . Therefore, the expansion can be used to show that at large times:

$$\log P_t(\vec{x}) = C + \frac{e^{-t}}{\Delta_t} \sum_{i=1}^d x_i \langle a_i \rangle - \frac{1}{2\Delta_t} \sum_{i,j=1}^d x_i M_{ij} x_j + O\left((xe^{-t})^3\right),$$

where  $C$  is an  $\vec{x}$ -independent term and

$$M_{ij} = \delta_{ij} - e^{-2t} \left[ \langle a_i a_j \rangle - \langle a_i \rangle \langle a_j \rangle \right].$$

The curvature of  $\log P_t(\vec{x})$  is closely linked to the spectral properties of the matrix  $M$ . In the large time regime,  $M$  approaches the identity matrix, and consequently, all its eigenvalues are positive. However, a qualitative shift in shape occurs at the maximum time  $t_s$ , where the largest eigenvalue of  $M$  transitions through zero. This marks the onset of the **speciation time**, distinguished by a change in curvature of the effective potential  $-\log P_t(\vec{x})$ . In this case, it can be easily computed: the matrix  $M$  is given by  $M_{ij} = (1 - \sigma^2 e^{-2t}) \delta_{ij} - e^{-2t} m_i m_j$  and its largest eigenvalue is  $(1 - \sigma^2 e^{-2t} - d\tilde{\mu}^2 e^{-2t})$ . We get therefore in the large  $d$  limit  $t_s = \frac{1}{2} \log(d\tilde{\mu}^2)$  which up to subleading corrections identifies the speciation timescale as

$$t_s = \frac{1}{2} \log(d).$$

## A.1 Asymptotic stochastic process in Regime I and symmetry breaking

In the limit of large dimensions, a comprehensive analytical examination of the dynamics in Regime I, taking place on time-scales  $t_s + O(1) = (1/2) \log d + O(1)$ , can be provided, specifically at the beginning of the backward process. Assuming no collapse (for further details, refer to Biroli et al. (2024)), an investigation into diffusion dynamics shows that the empirical distribution  $P_t^e(\vec{x})$  at time  $t$  can be approximated with high accuracy by  $P_t(\vec{x})$ . This approximation represents the convolution of the initial distribution  $P_0$ , comprising a mixture of Gaussians centered at  $\pm\vec{m}$ , and a diffusion kernel proportional to  $e^{-(\vec{x}-\vec{a}e^{-t})^2/2}$ . Consequently, the explicit expression for this approximation is

$$P_0(\vec{x}) = \frac{1}{2 \left(\sqrt{2\pi\sigma^2}\right)^d} \left[ e^{-(\vec{x}-\vec{m})^2/(2\sigma^2)} + e^{-(\vec{x}+\vec{m})^2/(2\sigma^2)} \right], \text{ and} \quad (10)$$

$$P_t(\vec{x}) = \frac{1}{2 \left(\sqrt{2\pi\Gamma_t}\right)^d} \left[ e^{-(\vec{x}-\vec{m}e^{-t})^2/(2\Gamma_t)} + e^{-(\vec{x}+\vec{m}e^{-t})^2/(2\Gamma_t)} \right]$$

where  $\Gamma_t = \sigma^2 e^{-2t} + \Delta_t$  goes to 1 at large times. The log of this probability is

$$\log P_t(\vec{x}) = -\frac{\vec{x}^2}{2\Gamma_t} + \log \cosh \left( \vec{x} \cdot \vec{m} \frac{e^{-t}}{\Gamma_t} \right),$$

and hence the score reads

$$S_t^i(\vec{x}) = -\frac{x^i}{\Gamma_t} + m_i \frac{e^{-t}}{\Gamma_t} \tanh \left( \vec{x} \cdot \vec{m} \frac{e^{-t}}{\Gamma_t} \right). \quad (11)$$

As there are two classes:  $+\vec{m}$  and  $-\vec{m}$ , the score conditioned to one class equals the score associated to a given Gaussian. Therefore, for the two classes we have:

$$\begin{aligned} +\vec{m} : S_t^i(\vec{x}, +) &= \frac{-x^i + m_i e^{-t}}{\Gamma_t}, \text{ and} \\ -\vec{m} : S_t^i(\vec{x}, -) &= \frac{-x^i - m_i e^{-t}}{\Gamma_t}. \end{aligned} \quad (12)$$

## A.2 When does classifier-free guidance take effect?

We can proceed to answer this question by examining the classifier-free guidance score, as defined in [Ho and Salimans \(2022\)](#):

$$S_{t_{CFG}}^i(\vec{x}, c) = (1 + \omega) S_t^i(\vec{x}, c) - \omega S_t^i(\vec{x}), \quad (13)$$

where  $c = \pm 1$  and  $\omega > 0$ . By plugging in the conditional (12) and unconditional scores (11), we can obtain:

$$\begin{aligned} S_{t_{CFG}}^i(\vec{x}, c) &= -\frac{x^i}{\Gamma_t} + (1 + \omega) \frac{cm_i e^{-t}}{\Gamma_t} - \omega \frac{m_i e^{-t}}{\Gamma_t} \tanh \left( \frac{\vec{x} \cdot \vec{m} e^{-t}}{\Gamma_t} \right) \\ &= -\frac{x^i}{\Gamma_t} + \omega \frac{m_i e^{-t}}{\Gamma_t} \left\{ c - \tanh \left( \frac{\vec{x} \cdot \vec{m} e^{-t}}{\Gamma_t} \right) \right\} + \frac{cm_i e^t}{\Gamma_t}. \end{aligned} \quad (14)$$

Now, in Regime II, when the trajectory has committed to a given class,  $\vec{x} \cdot \vec{m} \sim O(d)$  and  $\text{sign}(\vec{x} \cdot \vec{m}) = c$ . Therefore,  $c - \tanh \left( \frac{\vec{x} \cdot \vec{m} e^{-t}}{\Gamma_t} \right) \approx 0$ , and one finds from (14), that  $S_{t_{CFG}}^i(\vec{x}, c) = S_t^i(\vec{x})$ . This implies that, within this regime, classifier free guidance equals the conditional score. Therefore, Classifier free-guidance only affects Regime I, as  $S_{t_{CFG}}^i(\vec{x}, c) = S_t^i(\vec{x})$  for  $t > t_s = \frac{1}{2} \log(d)$ . This allows us to conclude one of the two results:

*Result 1.* In Regime II, CFG is innocuous.

## A.3 What is the role of classifier-free guidance?

Let us first analyze the ‘‘transverse’’ directions  $\vec{v} \perp \vec{m}$ . For these directions, for all  $\omega$ , the score is the same and equals  $\vec{S}_t^{CFG}(\vec{x}, c) \cdot \vec{v} = -\frac{\vec{x} \cdot \vec{v}}{\Gamma_t}$ . Let us project the backward Eq. (2) on a unit vector  $\vec{v} \perp \vec{m}$ . We write  $p = \vec{x} \cdot \vec{v}$ , and the backward equation now reads  $dp = p(1 - 2/\Gamma_{t_f - \tau})d\tau + \sqrt{2}dB$  which is the backward equation for a single Gaussian variable. When  $\tau \rightarrow t_f$  the projection  $p = \vec{x} \cdot \vec{v}$  is thus distributed as  $\mathcal{N}(0, \sigma^2)$ , for all values of  $\omega$ .

Therefore, as all the components except the one in the  $\vec{m}$  direction are not affected, we can consider only the component along  $\vec{m}$ :

$$\vec{S}_{t_{CFG}}(\vec{x}, c) \cdot \frac{\vec{m}}{|\vec{m}|} = -\frac{\vec{x} \cdot \vec{m} / |\vec{m}|}{\Gamma_t} + \omega \frac{|\vec{m}|^2 e^{-t}}{|\vec{m}| \Gamma_t} \cdot \left\{ c - \tanh \left( \frac{\vec{x} \cdot \vec{m} e^{-t}}{\Gamma_t} \right) \right\} + \frac{|\vec{m}| e^{-t} c}{\Gamma_t}.$$

By denoting  $\frac{\vec{x} \cdot \vec{m}}{|\vec{m}|} = q(t)$ , where  $|\vec{m}| = \sqrt{d}$ , we can obtain the backward equation:

$$dx^i = (x^i + 2S_{\tau_{CFG}}^i) d\tau + d\eta_i(\tau),$$

where  $\tau = t_f - t$ , i.e., the backward time. Therefore, we can obtain for Regime I and by projecting onto the  $\frac{\vec{m}}{|\vec{m}|}$  direction, we have that:

$$dq = dx^i \cdot \frac{\vec{m}}{|\vec{m}|} = \left( q + 2 \left[ -q + e^{-(t_f - t_s - \tau)} \left( (1 + \omega) - \omega \tanh \left( q e^{-(t_f - t_s - \tau)} \right) \right) \right] \right) d\tau + d\eta(\tau),$$

as, in Regime I, we have that  $\Gamma_t \approx 1$ , and also  $\sqrt{d} = e^{-t_s}$ .

Again, from this point onward by  $t(\tau)$  we denote the backward time for ease of notation. This is like having an effective potential:

$$dq = -\frac{\partial V^{CFG}(q, \tau)}{\partial q} d\tau + d\eta(\tau),$$

where

$$\begin{aligned} V^{CFG} &= \frac{1}{2} q^2 + 2 \left[ -(1 + \omega) c q e^{-(t-t_s)} + \omega \ln \cosh \left( q e^{-(t-t_s)} \right) \right] \\ &= \underbrace{\left( \frac{1}{2} q^2 - 2 e^{-(t-t_s)} c q \right)}_{\text{Classifier's potential}} + \omega \underbrace{\left[ -c q e^{-(t-t_s)} + \ln \cosh \left( q e^{-(t-t_s)} \right) \right]}_{\text{Extra potential } V_{\text{extra}}}. \end{aligned}$$

Therefore, for class  $c = +1$  (equivalently for  $c = -1$ ), there is little effect for  $q e^{-(t-t_s)} \gg 1$ , as then  $-q e^{-(t-t_s)} + \ln \cosh \left( q e^{-(t-t_s)} \right) \approx 0$ . Instead, for  $q e^{-(t-t_s)} \ll -1$ , we have that  $-q e^{-(t-t_s)} + \ln \cosh \left( q e^{-(t-t_s)} \right) \approx -q e^{-(t-t_s)} \gg 1$ . Therefore, we can conclude our remaining result:

*Result 2.* In Regime I, the effect of CFG is to push in the correct direction (corresponding to class  $c$ ).

The utility of CFG is therefore to "push" in the right direction in Regime I where arguably the class-based score/potential is likely not accurate in the rare region ( $q > 0$  for  $c = -1$  and  $q < 0$  for  $c = +1$ ). The behavior of the two potentials is displayed in Figure 7.

## B Experimental details: Gaussian mixtures

In this section, we present experimental details for the numerical simulations involving Gaussian mixtures, describing the procedures and the hyperparameter configurations.

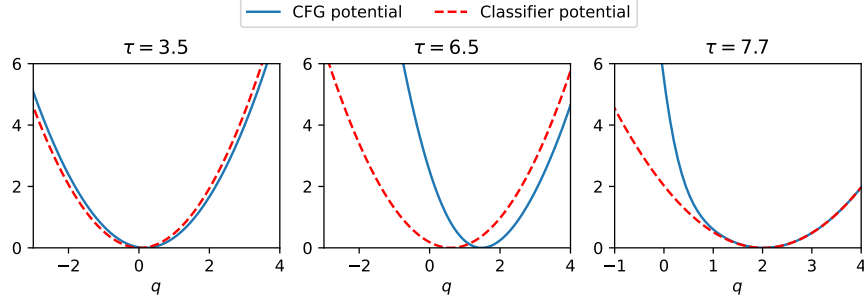


**Figure 7** The evolution of the conditional classifier potential, and the CFG potential during the backward process, as a function of backward time  $\tau$ . We can see the faster convergence to the target of the CFG, as well as the increased "narrowness" of the potential, leading to reduced variance of the generated distribution.

*Numerical simulations.* In the case of a mixture of two Gaussian clusters centered on  $\pm \vec{m} \in \mathbb{R}^d$  with variance  $\sigma^2$ , the score function reads as

$$S_{t_{CFG}}(\vec{x}(t), c) = -\frac{x(t)}{\Gamma_t} + \omega \frac{\vec{m}e^{-t}}{\Gamma_t} \left\{ c - \tanh \left( \frac{\vec{x}(t) \cdot \vec{m}e^{-t}}{\Gamma_t} \right) \right\} + \frac{c\vec{m}e^t}{\Gamma_t}.$$

where  $\Gamma_t = \Delta_t + \sigma^2 e^{-2t}$ , with  $\Delta_t = 1 - e^{-2t}$ . We can then discretize the stochastic differential equation associated to the backward process as

$$\vec{x}(t+1) = \vec{x}(t) + \eta [\vec{x}(t) + 2S_{t_{CFG}}(\vec{x}(t), c)] + \vec{\eta} \sqrt{2\tau/L}$$

where  $\vec{\eta} \sim \mathcal{N}(0, I)$ , with  $t_f = 8$  the time horizon and  $t_f/L = 0.01$ . We use  $\vec{m} = [1, \dots, 1]$ ,  $\sigma^2 = 1$ , and each point is obtained by averaging over 100 initial conditions. The speciation time  $t_s$  is calculated as  $t_s = -\frac{1}{2} \log d$ . Throughout the experiments, we plot the evolution of  $q(t) = \frac{\vec{x} \cdot \vec{m}}{|\vec{m}|}$ , conditioning the guidance on the positive class with  $c = 1$ .

Furthermore, we can observe the flexibility of the non-linear guidance in Figure 8, where we plot the distance between the conditional and unconditional score for linear (standard) and proposed non-linear, Power-Law version of CFG. We average over 5000 samples with  $\sigma^2 = 1$ ,  $\omega = 4$ , and for non-linear versions  $d = 50$  and  $\alpha \in \{0, -0.25, -0.5, -0.75, -0.9\}$ ,  $\gamma \in \{0, 2, 4, 8, 16\}$ . Across various hyperparameter configurations and CFG versions, the score difference is consistently zero at the beginning and end of the backward process.

## C Finite dimension

In this section, we give exact analyses describing the effect of CFG in finite- (possibly low-) dimensional settings, outlined in Section 4.4 in the main manuscript. We start the backward equation at a time  $t_f$  large enough that the distribution of  $x$  is a isotropic Gaussian with variance one. The backward equation for  $x(t)$  with the CFG score reads:

$$\begin{aligned} \frac{dx_i}{d\tau} = & x_i \left( 1 - \frac{2}{\Gamma(t_f - \tau)} \right) + \frac{2m_i}{\Gamma(t_f - \tau)} e^{-(t_f - \tau)} \\ & + 2\omega m_i \frac{e^{-(t_f - \tau)}}{\Gamma_{t_f - \tau}} \left\{ 1 - \tanh \left( \frac{\vec{x} \cdot \vec{m} e^{-(t_f - \tau)}}{\Gamma_{t_f - \tau}} \right) \right\} + \eta_i(\tau) \end{aligned} \quad (15)$$

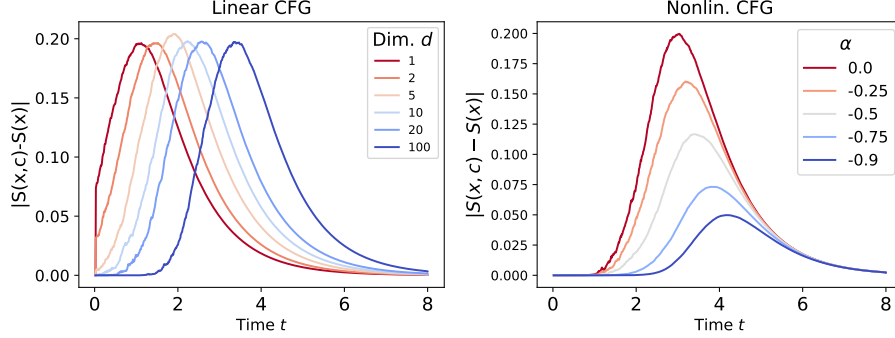


**Figure 8 CFG is innocuous in Regime II.** The distance between conditional and unconditional score for linear and two proposed non-linear versions of CFG, averaged over 5000 samples with  $\sigma^2 = 1$ ,  $\omega = 4$ , and for non-linear versions  $d = 50$  and  $\alpha \in \{0, -0.25, -0.5, -0.75, -0.9\}$ ,  $\gamma \in \{0, 2, 4, 8, 16\}$ . Across various hyperparameter configurations and CFG versions, the score difference is consistently zero at the beginning and end of the backward process.

where  $\tau = 0$  at the beginning of the backward process and  $\tau = t_f (\gg 1)$  at the end.

This can be projected on the evolution of the single parameter  $q(\tau) = \vec{x} \cdot \vec{m} / \sqrt{d}$ . We obtain

$$\begin{aligned} \frac{dq}{d\tau} = & q \left( 1 - \frac{2}{\Gamma(t_f - \tau)} \right) + \frac{2\sqrt{d}}{\Gamma(t_f - \tau)} e^{-(t_f - \tau)} \\ & + 2\omega\sqrt{d} \frac{e^{-(t_f - \tau)}}{\Gamma_{t_f - \tau}} \left\{ 1 - \tanh \left( \frac{q\sqrt{d}e^{-(t_f - \tau)}}{\Gamma_{t_f - \tau}} \right) \right\} + \eta(\tau). \end{aligned} \quad (16)$$

Considering the right-hand side as a force due to a moving external potential  $-\partial_q V(q, t)$ , the effect of CFG is to add an extra term which has two main effects: (1) it adds a positive term to the force and, in consequence, it pushes  $q$  faster away from zero, (2) it increases the value of the Hessian at any point in  $q$  with respect to its  $\omega = 0$  counterpart, thus making the potential more confining.

The initial condition is  $q(\tau = 0) \sim \mathcal{N}(0, \sigma^2)$  and

$$\Gamma(t_f - \tau) = \sigma^2 e^{-2(t_f - \tau)} + 1 - e^{-2(t_f - \tau)}. \quad (17)$$

**Case:**  $\omega = 0$

The solution of the backward equation is:

$$q(\tau) = q(0) e^{\tau - 2 \int_0^\tau \frac{1}{\Gamma(t_f - \tau'')} d\tau''} + \int_0^\tau \left[ \frac{2\sqrt{d}e^{-(t_f - \tau')}}{\Gamma(t_f - \tau')} + \eta_i(\tau') \right] e^{(\tau - \tau') - 2 \int_{\tau'}^\tau \frac{1}{\Gamma(t_f - \tau'')} d\tau''} d\tau'. \quad (18)$$

Its probability distribution must coincide with the one of the solutions of the forward equation, which reads:

$$q(t) = \sqrt{d}e^{-t} + \sqrt{1 - e^{-2t}} z_i + e^{-t} \sigma \tilde{z}_i,$$

where  $z_i, \tilde{z}_i \sim \mathcal{N}(0, 1)$  and  $t = t_f - \tau$ . Let us now focus on the mean of  $q$ . When we consider the term

$$\int_0^\tau \left[ \frac{2\sqrt{d}e^{-(t_f - \tau')}}{\Gamma(t_f - \tau')} \right] e^{(\tau - \tau') - 2 \int_{\tau'}^\tau \frac{1}{\Gamma(t_f - \tau'')} d\tau''} d\tau',$$

using that

$$\frac{d}{d\tau'} \exp \left[ -2 \int_{\tau'}^\tau \frac{1}{\Gamma(t_f - \tau'')} d\tau'' \right] = \frac{2}{\Gamma(t_f - \tau')} \exp \left[ -2 \int_{\tau'}^\tau \frac{1}{\Gamma(t_f - \tau'')} d\tau'' \right],$$

one finds that the mean of  $q$  for the evolution with  $\omega = 0$ , starting from any value  $q(0)$  at any time  $t_f$ , is

$$q(\tau) = q(0)e^{\tau-2\int_0^\tau \frac{1}{\Gamma(t_f-\tau')}d\tau'} + \sqrt{d}e^{-(t_f-\tau)} \left( 1 - \exp \left( -2 \int_0^\tau \frac{1}{\Gamma(t_f-\tau')}d\tau' \right) \right). \quad (19)$$

Using

$$\int_0^\tau \frac{1}{\Gamma(t_f-\tau')}d\tau' = -\frac{1}{2} \log \frac{e^{-2\tau} + (\sigma^2 - 1)e^{-2t_f}}{1 + (\sigma^2 - 1)e^{-2t_f}},$$

we find that

$$q(\tau) = q(0) e^\tau \frac{e^{-2\tau} + (\sigma^2 - 1)e^{-2t_f}}{1 + (\sigma^2 - 1)e^{-2t_f}} + \sqrt{d} e^{-(t_f-\tau)} \frac{1 - e^{-2\tau}}{1 + (\sigma^2 - 1)e^{-2t_f}}. \quad (20)$$

One can check that, when  $q(0)$  is obtained by the equilibrium process with  $\omega = 0$ , namely  $q(0) = \sqrt{d}e^{-t_f}$ , then at all times  $q(\tau) = \sqrt{d}e^{-(t_f-\tau)}$ .

### Case: interrupted guidance

Now let us consider a protocol of interrupted guidance. We start the backward process at  $t_f \gg 1$  with a CFG coefficient  $\omega > 0$ . Then at time backward time  $\tau_1$  (forward time  $t_1 = t_f - \tau_1$ ) we switch to  $\omega = 0$ . At time  $t_1$  the mean of  $q$  obtained from the backward process with  $\omega > 0$  is larger than the value  $\sqrt{d}e^{-t_1}$  which would be obtained with the  $\omega = 0$  dynamics (the reason is that the extra force in (16) is positive). Let us write this mean as

$$q(t_1, \omega) = \sqrt{d} e^{-t_1} + \delta q(t_1, \omega).$$

Let us measure the backward time starting from  $t = t_1$ . We thus write  $t = t_1 - \tilde{\tau}$ . We can use formula (20) with  $t_f \rightarrow t_1$ ,  $\tau \rightarrow \tilde{\tau}$  and  $q(0) \rightarrow q(t_1, \omega)$ . This gives for the mean value of  $q$ :

$$\tilde{q}(\tilde{\tau}, \omega) = \sqrt{d}e^{-(t_1-\tilde{\tau})} + \delta q(t_1, \omega) \frac{e^{-\tilde{\tau}} + (\sigma^2 - 1)e^{\tilde{\tau}-2t_1}}{1 + (\sigma^2 - 1)e^{-2t_1}},$$

which, translated in terms of the forward time  $t = t_1 - \tilde{\tau}$ , gives:

$$q(t) = \sqrt{d}e^{-t} + \delta q(t_1, \omega) e^{t-t_1} \frac{1 + (\sigma^2 - 1)e^{-2t}}{1 + (\sigma^2 - 1)e^{-2t_1}}. \quad (21)$$

In particular at the end of the backward process, for  $\tilde{\tau} = t_1$  we get

$$q(t=0) = \sqrt{d} + \delta q(t_1, \omega) e^{-t_1} \frac{\sigma^2}{1 + (\sigma^2 - 1)e^{-2t_1}}$$

If we choose  $t_1 = t_s = (1/2) \log d$ , and assuming that the dynamics at  $t > t_1$  has produced an average  $q(t_1) = \sqrt{d}e^{-t_1} + \delta q$ , we find that

$$q(t=0) = \sqrt{d} \left( 1 + \delta q \frac{\sigma^2/d}{1 + (\sigma^2 - 1)/d} \right).$$

This shows that the guidance interrupted at  $t_s$  gives a good result only in the limit  $\sigma^2/d \ll 1$ . Figs. 9 and 10 illustrate the effect of the choice of  $t_1$ .

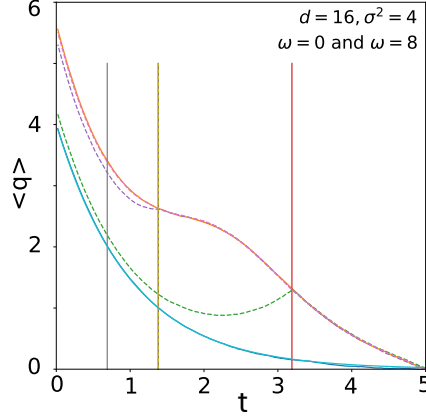


**Figure 9** Mean value of  $q$  obtained from the backward diffusion in a Gaussian mixture model with  $d = 16, \sigma^2 = 4$  (speciation time  $t_s = 1.38$ ). The CFG is run with  $\omega = 8$  from  $t = 5$  to  $t = t_1$ , then one switches to the class guidance  $\omega = 0$ . The top curve is when CFG is kept all the time ( $t_1 = 0$ ). The bottom curve is the case without CFG ( $\omega = 0$ ). Three values of  $t_1$  are studied  $t_1 = 0.69, 1.38, 3.19$  (vertical lines). The dashed curves give the mean value of  $q$  for each of these three cases. They are in perfect agreement with the theoretical prediction (21).

### CFG contribution to the magnetization in Regime I

Using Equation (14), one can derive the equation for the average  $\langle q(\tau) \rangle_\omega$ :

$$\begin{aligned} \frac{d\langle q(\tau) \rangle_\omega}{d\tau} &= \langle q(\tau) \rangle_\omega \left( 1 - \frac{2}{\Gamma(t_f - \tau)} \right) + \frac{2\sqrt{d}}{\Gamma(t_f - \tau)} e^{-(t_f - \tau)} \\ &+ 2\omega\sqrt{d} \frac{e^{-(t_f - \tau)}}{\Gamma(t_f - \tau)} \left\langle 1 - \tanh \left( \frac{q\sqrt{d}e^{-(t_f - \tau)}}{\Gamma(t_f - \tau)} \right) \right\rangle_\omega. \end{aligned} \quad (22)$$

The extra  $\omega$  term is strictly positive. Therefore, we have:

$$\langle q(\tau) \rangle_\omega \geq \langle q(\tau) \rangle_{\omega=0}, \quad \forall \tau.$$

Moreover, using that the right-hand side is less than or equal to:

$$\langle q(\tau) \rangle_\omega \left( 1 - \frac{2}{\Gamma(t_f - \tau)} \right) + \frac{2(1 + \omega)\sqrt{d}}{\Gamma(t_f - \tau)} e^{-(t_f - \tau)},$$

which corresponds to the backward equation one would obtain if  $\|\vec{m}\|^2 = (1 + \omega)d$ . We then find:

$$\langle q(\tau) \rangle_{\omega=0} < \langle q(\tau) \rangle_\omega < \sqrt{d}e^{-t}(1 + \omega).$$

We conclude that  $\langle q(\tau) \rangle_\omega$  gets an extra contribution due to CFG of the order  $\sqrt{d}e^{-t}$ .

CFG indeed shifts the mean value. The amount of shift is of order  $\sqrt{d}e^{-t}$  in Regime I. However, as we shall see next the CFG has almost no effect in Regime II, so we can use the result of the previous section to argue that the total shift due to CFG is the one of CFG in Regime I followed by a switch at  $\omega = 0$  in Regime II, i.e., it is of order one.

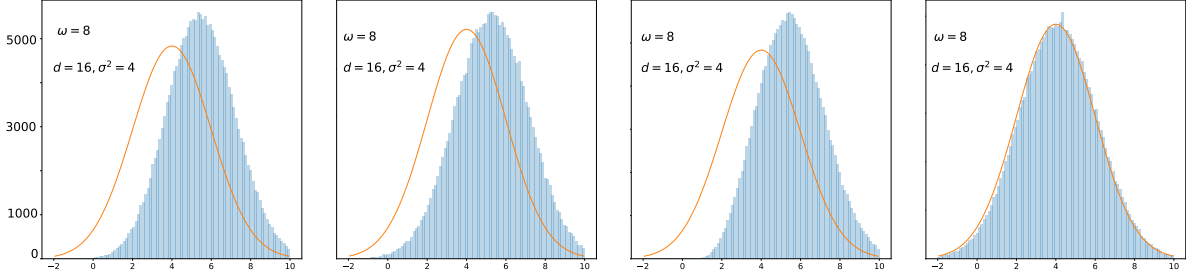


**Figure 10** Histograms of  $q(t=0)$  obtained from the backward diffusion in a Gaussian mixture model with  $d = 16, \sigma^2 = 4$  (the speciation time is 1.38), run with 200,000 trajectories. Left: CFG with  $\omega = 8$  is applied at all times. The final distribution has a larger mean and a smaller variance than the desired class distribution (full line). Next three figures: The CFG is run with  $\omega = 8$  from  $t = 5$  to  $t = t_1$ , then one switches to standard CFG  $\omega = 0$ . From left to right,  $t_1 = 0.69, 1.38, 3.19$ . The mean values of  $q$  in the four cases are respectively 5.56, 5.51, 5.29, 4.12 and the standard deviations 1.68, 1.74, 1.87, 1.98, with targets  $\mu = 4, \sigma = 2$ . In order to minimize the bias due to CFG one must interrupt it before the speciation takes place in the background diffusion, hence at  $t_1 > t_s$ .

## CFG contribution to the score in Regime I vs in Regime II

Another interesting inequality can be derived for the difference between the CFG and the standard, non-guided score,  $S_{\text{CFG}} - S_C$ , evaluated on trajectories corresponding to CFG:

$$S_{\text{CFG}} - S_C = \omega \frac{\sqrt{d}e^{-(t_f-\tau)}}{\Gamma(t_f-\tau)} \left( 1 - \tanh \left( \frac{q\sqrt{d}e^{-(t_f-\tau)}}{\Gamma(t_f-\tau)} \right) \right). \quad (23)$$

We use the fact that for the same thermal noise, we have  $q_\omega(\tau) \geq q_{\omega=0}(\tau)$  because the CFG force is always equal or larger than the  $\omega = 0$  one. Therefore for a given (the same) thermal history we have:

$$-\tanh \left( \frac{q_\omega(\tau)\sqrt{d}e^{-(t_f-\tau)}}{\Gamma(t_f-\tau)} \right) \leq -\tanh \left( \frac{q_{\omega=0}(\tau)\sqrt{d}e^{-(t_f-\tau)}}{\Gamma(t_f-\tau)} \right), \quad (24)$$

and we can obtain:

$$S_{\text{CFG}} - S_C \leq \frac{\sqrt{d}e^{-(t_f-\tau)}}{\Gamma(t_f-\tau)} \left( 1 - \tanh \left( \frac{q_{\omega=0}(\tau)\sqrt{d}e^{-(t_f-\tau)}}{\Gamma(t_f-\tau)} \right) \right). \quad (25)$$

This inequality tells us, as expected, that the extra CFG contribution to the score is very small at the beginning of the backward process. Its mean increases, and is of the order of one during the backward process in Regime I. However, after the speciation time  $q_{\omega=0}(\tau)$  is a Gaussian variable with a mean  $\sqrt{d}e^{-(t_f-\tau)}$  much larger than the square root of the variance. Therefore, replacing the fluctuating variable by its mean we obtain

$$S_{\text{CFG}} - S_C \leq \frac{\sqrt{d}e^{-(t_f-\tau)}}{\Gamma(t_f-\tau)} \left( 1 - \tanh \left( \frac{de^{-2(t_f-\tau)}}{\Gamma(t_f-\tau)} \right) \right). \quad (26)$$

In Regime II,  $t_f - \tau$  is of order one, and using the asymptotic form of the hyperbolic tangent one finds that

$$S_{\text{CFG}} - S_C \leq \frac{\sqrt{d}e^{-(t_f-\tau)}}{\Gamma(t_f-\tau)} \exp \left( -2 \frac{de^{-2(t_f-\tau)}}{\Gamma(t_f-\tau)} \right). \quad (27)$$

Therefore in Regime II the extra contribution to the score is exponentially small in  $d$  and its effect is completely negligible with respect to the one in Regime I.

## Analysis of the CFG effect on the variance

Let us derive the equation for  $\langle q^2(\tau) \rangle_\omega - \langle q(\tau) \rangle_\omega^2$ .

Using Itô calculus, we have (multiplying by  $q(\tau)$  in the equation for  $\frac{dq(\tau)}{d\tau}$ ):

$$\begin{aligned} \frac{dq^2(\tau)}{d\tau} &= 2 + 2q^2(\tau) \left( 1 - \frac{2}{\Gamma(t_f - \tau)} \right) + 2q(\tau) \frac{2\sqrt{d}}{\Gamma(t_f - \tau)} e^{-(t_f - \tau)} \\ &\quad + 2 \frac{2\omega\sqrt{d}}{\Gamma(t_f - \tau)} e^{-(t_f - \tau)} \left( q(\tau) - q(\tau) \tanh \left( \frac{q(\tau)\sqrt{d}e^{-(t_f - \tau)}}{\Gamma(t_f - \tau)} \right) \right) \\ &\quad + 2q(\tau)\eta(\tau). \end{aligned} \tag{28}$$

Taking the average and subtracting  $2\langle q(\tau) \rangle_\omega \frac{d\langle q(\tau) \rangle_\omega}{d\tau}$ , we find the equation for  $\langle q^2(\tau) \rangle_\omega - \langle q(\tau) \rangle_\omega^2$ :

$$\begin{aligned} \frac{d\langle q^2(\tau) \rangle_\omega - \langle q(\tau) \rangle_\omega^2}{d\tau} &= 2 + 2 \left( \langle q^2(\tau) \rangle_\omega - \langle q(\tau) \rangle_\omega^2 \right) \left( 1 - \frac{2}{\Gamma(t_f - \tau)} \right) \\ &\quad + \omega \frac{4\sqrt{d}e^{-(t_f - \tau)}}{\Gamma(t_f - \tau)} \left( \langle q(\tau) \rangle_\omega \left\langle \tanh \left( \frac{q\sqrt{d}e^{-(t_f - \tau)}}{\Gamma(t_f - \tau)} \right) \right\rangle_\omega \right. \\ &\quad \left. - \langle q(\tau) \tanh \left( \frac{q\sqrt{d}e^{-(t_f - \tau)}}{\Gamma(t_f - \tau)} \right) \rangle_\omega \right). \end{aligned} \tag{29}$$

At the beginning of the backward process, one can expand  $\tanh(x)$  and observe that the term in the parentheses is proportional to:

$$- \left( \langle q(\tau) \rangle_\omega^2 - \langle q(\tau) \rangle_\omega^2 \right), \tag{30}$$

which is negative. Therefore, we can conclude that the classifier-free-guidance-added term will result in shrinkage of the variance.

As for the mean, the main CFG effect on the variance is produced in Regime I, since the CFG score term is exponentially small in Regime II.

## D Real-world experiments

### D.1 Performing time reparameterization

In the second part of the paper, we evaluate the score of Diffusion Model with Transformers (DiT), in discrete time, as introduced by [Peebles and Xie \(2023\)](#). In this context, the forward process has a linear variance schedule  $\{\beta_t\}_{t'=1}^L$ , where  $L$  is the time horizon given as a number of steps. Here, the variance is evolving linearly from  $\beta_1 = 10^{-4}$  to  $\beta_{1000} = 2 \times 10^{-2}$ . A sample (without any guidance), at timestep  $t'$ , denoted  $\vec{x}(t')$  can therefore be expressed readily from its initial state,  $\vec{x}(0) = \vec{a}$ , as

$$\vec{x}(t') = \sqrt{\bar{\alpha}(t')} \vec{a} + \sqrt{1 - \bar{\alpha}(t')} \vec{\xi}(t')$$

where  $\bar{\alpha}(t') = \prod_{s=1}^{t'} (1 - \beta_s)$  and  $\xi$  is a standard and centered Gaussian noise. This equation in fact corresponds to the discretization of the Ornstein-Uhlenbeck Eq. (9) under the following reparameterization of the timestep  $t'$ ,

$$t = -\frac{1}{2} \log(\bar{\alpha}(t')),$$

where  $t$  is the time as defined in the main manuscript. This gives the map between the timescale used in our theoretical approach and numerical simulations of Gaussian mixtures, and the one used in our real-world settings. We note that, as the neural network predicts the noise, in order to calculate the score, one needs to normalize the output by the standard deviation (depending on the variance schedule). In this case, this corresponds to dividing the neural network output by  $\sigma(t') = \sqrt{1 - \bar{\alpha}(t')}$ . In numerical experiments, we divide by  $\sigma(t') + 1$  to avoid numerical errors. This is theoretically justified due to the fact that, as discussed in main paper, the score difference  $|S_{t'}(\vec{x}, c) - S_{t'}(\vec{x})|$  for large forward times decays exponentially (as  $e^{-t'}$ ) to zero.

In addition, for completeness, we now present the full comparison of numerical simulations to real-world using the time-reparameterization to plot the timesteps on the same time-scale. Our findings are portrayed in Figure 11. As each framework uses a separate time reparameterization, the x-axis needs to be recalculated accordingly. For the EDM2 framework (Karras et al., 2022), this can be done as follows: given a noise schedule  $\sigma(t)$ , the reparameterization can be calculated as  $t'(t) = (1/2) \log(1 + \sigma^2(t))$ , assuming that  $s(t) = 1$ . For the case  $s(t)$ , one needs to resort to equation Eq. (2).

## D.2 Hyperparameter configurations

Here, we give exact hyperparameters used for reproducing all our experiments.

In **Figure 1**, we plot the histograms of the samples generated using the backward process with dimensions  $d \in \{2, 200\}$  and guidance parameter  $\omega \in \{0, 0.2, 15\}$ , with  $\sigma^2 = 1$ , averaged over 10,000 trajectories.

In **Figure 2**, we plot the evolution of the 1D backward dynamics with means at  $\pm 4$  and unit variance. The potential plotted corresponds to equation  $V(q, t) = \frac{1}{2}q^2 - 2 \log \cosh(qe^{-(t-t_s)})$ . For the derivation of this potential, see Appendix B.2 in Biroli et al. (2024).

In **Figure 3**, we examine the following functions:

$$\begin{aligned} V_{\text{class}}(q, t; c) &= \frac{1}{2}q^2 - ce^{-(t-t_s)}q + 2 \\ V_{\text{extra}}(q, t; c) &= -ce^{-(t-t_s)}q + \log\left(\cosh\left(qe^{-(t-t_s)}\right)\right) + \log(2), \end{aligned}$$

where the plots correspond to  $V_{\text{class}}$ ,  $V_{\text{extr}}$  and  $(V_{\text{class}} + \omega V_{\text{extr}})$  with  $\omega = 3$  respectively. We select  $c = 1$ , and fix the speciation time to  $t_s = .5$ . The additive constants are manually added for clarity of presentation.

In **Figure 4**, we examine the evolution of the mean of  $q(t)$ . We set  $d = 1000$  (therefore  $t_s = 2$ ), with  $\sigma^2 = 1$ . and average over 10,000 trajectories.

In **left part of Figure 5**, we evaluate the difference of the conditional and unconditional score for Gaussian mixtures,  $|S_t(x, c) - S_t(x)|$  for dimensions  $d \in \{10, 100\}$  with 2,4 and 8 classes, using  $\omega = 4$ ,  $\sigma^2 = 1$ , averaged over 10,000 trajectories. The eight Gaussians are centered to be on equidistant means on a sphere with radius  $r = \sqrt{d}$ .

In **right part of Figure 5**, we plot the score difference for four real-world models: DiT/XL-2, EDM2-S, MMDiT and MDTv2, all trained using the diffusion objective. As each of the models' default hyperparameters have different number of sampling steps, we normalize the x-axis from 0 to 1: e.g., DiT framework uses 250 sampling steps, EDM2 uses 32 and for the text-to-image models we use 50 sampling steps. The y-axis is normalized to be between 0 and 1 for easier readability. All hyperparameters are set to the default ones.

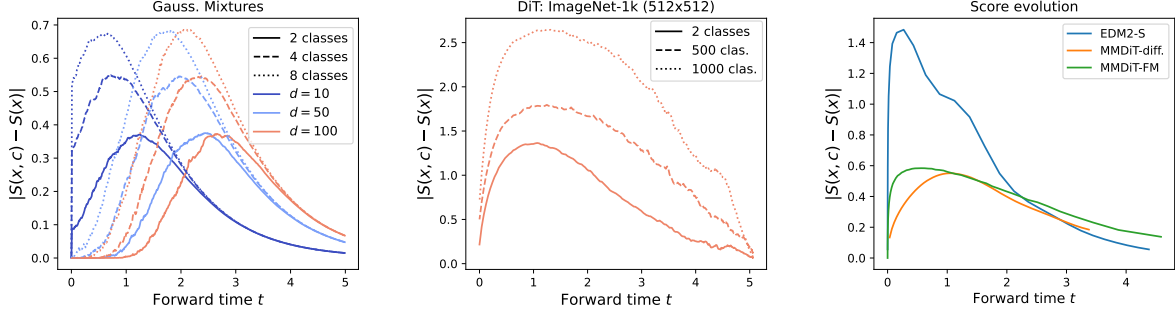


**Figure 11 Evolution of the score differences for numerical simulations and real-world experiments** projected onto the same time-scale for direct comparison. **First:** Numerically simulating mixture of two, four, and eight Gaussians with equidistant means on a sphere ( $r = \sqrt{d}$ ), with varying dimension  $d$ , with  $\omega = 4, \sigma^2 = 1$ , averaged over 10,000 trajectories. As  $d$  increases, the score difference starts to increase at an earlier backward time  $\tau$ . Additionally, as the number of classes increases, the magnitude of the score difference grows, as well as the duration of large difference between the scores. **Second:** Three DiT/XL-2 models trained on ImageNet-1K using 2, 500, and 1000 classes (image size  $512 \times 512$ ). We observe a similar pattern: as  $d$  increases, the score difference becomes larger at an earlier time. Furthermore, as the number of classes increases, the magnitude of the score difference increases, together with the duration for which the difference remains large. **Third:** evolution of the remaining models used in our experiments (EDM2-S, MMDiT and MDTv2). We observe a similar behavior to theory and the DiT/XL-2 models.

In **Figure 6**, we provide qualitative analysis of Standard and Power-Law CFG using DiT/XL-2 trained on ImageNet-1K ( $256 \times 256$ ) with  $\omega = 4$  in both cases and  $\alpha = 0.1$  in the non-linear version. All other hyperparameters are set to the default values.

In **Figure 7**, we use the same hyperparameter configuration as in **Figure 3**, plotting for various values of the backward time  $\tau$ : 3.5, 6.5 and 7.7.

In **Figure 8**, we plot the difference of conditional and unconditional score for standard and Power-Law CFG, averaged over 5,000 samples with  $\sigma^2 = 1, \omega = 4$ , and for non-linear version  $d = 50$  and  $\alpha \in \{0, -0.25, -0.5, -0.75, -0.9\}$ .

In **Figure 9**, we plot the backward diffusion in a Gaussian mixture model with  $d = 16, \sigma^2 = 4, \omega = 8$ . The CFG is either run at all times (top curve), stopped at times  $t_1$  or not used at all (bottom curve).

In **Figure 10**, we perform linear CFG with  $\omega = 8$  from  $t = 5$  to  $t = t_1$ , after which we turn CFG off ( $\omega = 0$ ) at times  $t_1 = 0.69, 1.38, 3.19$ .

In **Figure 11**, we perform the same experiment as in the left part of, however with DiT/XL-2 model trained on 2, 500 and 1000 classes. For 2 classes, we have selected the same classes as in [Biroli et al. \(2024\)](#), and for the 500 we selected the first 500 classes in ImageNet-1K. The x-axis represents the Forward time  $t$ , where the parameterization is obtained as explained in [App. D.1](#).

In **Figures 12-13**, we use  $d = 16$  and  $\sigma^2 = 4$ .

In the **first column** of **Figure 14**, we plot the estimated Jensen-Shannon Divergence between the target samples corresponding to a randomly selected class and the diffusion particles throughout the backward trajectory. Note that this is performed in latent space. For obtaining the **middle column**, we first take all data samples from one class, embed them into the latent space and calculate the centroid corresponding to this class. Then, we normalize the centroid (making it unit norm) and plot the dot product of the particles throughout the backward diffusion process with the calculated centroid. The **right column** corresponds to the score difference. Across all experiments, we selected  $\omega = 4$ , sampled using DDPM ([Ho et al., 2020](#)) using 250 sampling steps, averaged over 25 samples. All other hyperparameter configurations are set to the default.

Finally, in **Figure 15**, we perform the same experiment as in **Figure 5** right, however we do not normalize the x- nor the y-axis.

**Table 2** displays the hyperparameters used to obtain the results given in **Table 1**. The evaluation code relied

**Table 2** Hyperparameters used throughout our experiments. All other hyperparameters are set to the default values.

	param.	DiT/XL-2 <i>IM256</i>	EDM2-S <i>IM512</i>	MMDiT <i>CC12M</i>	MDTv2 <i>CC12M</i>	MMDiT-FM <i>COCO</i>
Stand.	$\omega$	1.5	1.4	1.6	1.5	1.65
Scheduler	$s, \omega$	1.6, 1.95	2, 3.5	0.1, 1.75	1.5, 2.0	0.5, 3.25
NL-Stand.	$\alpha, \omega$	-0.1, 1.6	-0.06, 2.35	0.15, 2.15	0.25, 1.75	0.3, 3.5
Limited	$\omega$	1.8	2.1	1.6	1.5	2.15
Lim. v2	$\omega$	1.85	2.0	1.7	1.6	2.25
NL-Lim.v2	$\alpha, \omega$	-0.03, 2.1	-0.05, 2.05	0.225, 2.55	0.2, 2.35	0.05, 3.25

on EvalGIM library by [Hall et al. \(2024\)](#). We observe that the optimal hyperparameter configuration aligns with the findings of [Kynkäänniemi et al. \(2024\)](#), which suggest that when guidance is applied over a shorter interval (analogous to non-linear CFG), a stronger or larger value of  $\omega$  is typically necessary for optimal performance.

## E Computation for the mixture of four Gaussians

Here we present the computation for a mixture of four Gaussians, in order to analyze the behavior of the system for increasing number of classes. As before, assuming no collapse, we can approximate the empirical distribution  $P_t^e(\vec{x})$  at time  $t$  by  $P_t(\vec{x})$  with high accuracy. In this case, the approximation represents the convolution of the initial distribution  $P_0$ , being a mixture of 4 Gaussians centered at  $\pm\vec{\mu}_1 \pm \vec{\mu}_2$ , s.t.  $\vec{\mu}_1 \cdot \vec{\mu}_2 = 0$ , and a diffusion kernel proportional to  $e^{-(\vec{x}-\vec{a}e^{-t})^2/2}$ . The explicit expression for the distribution is:

$$P_0(\vec{x}) = \frac{1}{4 \left(\sqrt{2\pi\sigma^2}\right)^d} \left[ e^{-(\vec{x}-(\vec{\mu}_1-\vec{\mu}_2))^2/(2\sigma^2)} + e^{-(\vec{x}-(\vec{\mu}_1+\vec{\mu}_2))^2/(2\sigma^2)} \right. \\ \left. + e^{-(\vec{x}+(\vec{\mu}_1-\vec{\mu}_2))^2/(2\sigma^2)} + e^{-(\vec{x}+(\vec{\mu}_1+\vec{\mu}_2))^2/(2\sigma^2)} \right]$$

and

$$P_t(\vec{x}) = \frac{1}{4 \left(\sqrt{2\pi\Gamma_t}\right)^d} \left[ e^{-(\vec{x}-(\vec{\mu}_1-\vec{\mu}_2)e^{-t})^2/(2\Gamma_t)} + e^{-(\vec{x}-(\vec{\mu}_1+\vec{\mu}_2)e^{-t})^2/(2\Gamma_t)} \right. \\ \left. + e^{-(\vec{x}+(\vec{\mu}_1-\vec{\mu}_2)e^{-t})^2/(2\Gamma_t)} + e^{-(\vec{x}+(\vec{\mu}_1+\vec{\mu}_2)e^{-t})^2/(2\Gamma_t)} \right]$$

where  $\Gamma_t = \sigma^2 e^{-2t} + \Delta_t$  goes to 1 at large times. This can be rewritten as:

$$P_t(\vec{x}) = \frac{1}{2 \left(\sqrt{2\pi\Gamma_t}\right)^d} e^{-(\vec{x}^2 + \vec{\mu}_1^2 e^{-2t} + \vec{\mu}_2^2 e^{-2t})/(2\Gamma_t)} \left[ e^{-\vec{\mu}_1 \cdot \vec{\mu}_2 e^{-2t}/\Gamma_t} \cosh\left(\vec{x} \cdot (\vec{\mu}_1 + \vec{\mu}_2) \frac{e^{-t}}{\Gamma_t}\right) \right. \\ \left. + e^{\vec{\mu}_1 \cdot \vec{\mu}_2 e^{-2t}/\Gamma_t} \cosh\left(\vec{x} \cdot (\vec{\mu}_1 - \vec{\mu}_2) \frac{e^{-t}}{\Gamma_t}\right) \right]$$

The log of this probability is:

$$\log P_t(\vec{x}) = \frac{-\vec{x}^2}{2\Gamma_t} + \log \left( e^{-\vec{\mu}_1 \cdot \vec{\mu}_2 e^{-2t}/\Gamma_t} \cosh \left( \vec{x} \cdot (\vec{\mu}_1 + \vec{\mu}_2) \frac{e^{-t}}{\Gamma_t} \right) + e^{\vec{\mu}_1 \cdot \vec{\mu}_2 e^{-2t}/\Gamma_t} \cosh \left( \vec{x} \cdot (\vec{\mu}_1 - \vec{\mu}_2) \frac{e^{-t}}{\Gamma_t} \right) \right)$$

And the score reads:

$$S_t^i(\vec{x}) = \frac{-x^i}{\Gamma_t} + \frac{e^{-t} (\vec{\mu}_1 + \vec{\mu}_2)_i e^{-\vec{\mu}_1 \cdot \vec{\mu}_2 e^{-2t}/\Gamma_t} \sinh \left( \vec{x} \cdot (\vec{\mu}_1 + \vec{\mu}_2) \frac{e^{-t}}{\Gamma_t} \right) + (\vec{\mu}_1 - \vec{\mu}_2)_i e^{\vec{\mu}_1 \cdot \vec{\mu}_2 e^{-2t}/\Gamma_t} \sinh \left( \vec{x} \cdot (\vec{\mu}_1 - \vec{\mu}_2) \frac{e^{-t}}{\Gamma_t} \right)}{e^{-\vec{\mu}_1 \cdot \vec{\mu}_2 e^{-2t}/\Gamma_t} \cosh \left( \vec{x} \cdot (\vec{\mu}_1 + \vec{\mu}_2) \frac{e^{-t}}{\Gamma_t} \right) + e^{\vec{\mu}_1 \cdot \vec{\mu}_2 e^{-2t}/\Gamma_t} \cosh \left( \vec{x} \cdot (\vec{\mu}_1 - \vec{\mu}_2) \frac{e^{-t}}{\Gamma_t} \right)}$$

As  $\vec{x}$  approaches one of the means  $\pm \vec{\mu}_1 \pm \vec{\mu}_2$ , the second summand reduces to  $(\vec{\mu}_1 \pm \vec{\mu}_2) \tanh \left( \vec{x} \cdot (\vec{\mu}_1 \pm \vec{\mu}_2) \frac{e^{-t}}{\Gamma_t} \right)^4$ , resulting in an expression akin to the one for mixture of 2 Gaussians in (11).

## F Further notes on non-linear CFG

Our first non-linear CFG, given by

$$S_{t_{CFG-NL}}(\vec{x}, c) = S_t(\vec{x}, c) + [S_t(\vec{x}, c) - S_t(\vec{x})] f(|S_t(\vec{x}, c) - S_t(\vec{x})|),$$

with  $f(x) = \omega x^\alpha$  and  $\alpha > -1$ , is generally used with  $\alpha$  negative or of small magnitude. This is very efficient at pushing the trajectories in the direction of the desired class at early times of the backward process. The reason is that, at large  $t$ , the scores  $S_t(\vec{x})$  and  $S_t(\vec{x}, c)$  go to zero as  $e^{-t}$ , and the non-linear term becomes large. However this effect also occurs when  $t < t_s$ , where the difference  $|S_t(\vec{x}, c) - S_t(\vec{x})|$  becomes small. Although in the regime of  $t \ll t_s$  the non-linear term does not matter, in the intermediate regime  $t$  close to  $t_s$  the strong non-linear term impacts the trajectory. In finite dimension it biases the distribution obtained at  $t = 0$  (see Fig.14).

One would like to have different non-linearities applying to the regimes  $t \gg t_s$  and  $t < t_s$ . One possibility is to use the following version.

*Rescaled Power-law CFG.* Here, by denoting with  $\langle \cdot \rangle$  the expectation w.r.t. the effective distribution  $P_0(\vec{a})e^{-\vec{a}^2 s(t)/(2s(t)^2 \sigma(t)^2)}$ , the score difference can be expressed as  $|\vec{S}_t(\vec{x}, c) - \vec{S}_t(\vec{x})| = (1/(s(t)\sigma(t)^2)) |\langle \vec{a} \rangle_{\vec{x}, c} - \langle \vec{a} \rangle_{\vec{x}}|$ , where  $s(t)$  and  $\sigma(t)$  are related to the functions  $f(t)$  and  $g(t)$  of Eq. (1) by  $s(t) = \exp \int_0^t d\tau f(\tau)$  and  $\sigma(t) = \int_0^t d\tau g(\tau)^2 / s(\tau)^2$ . Therefore the non-linear function depends on the difference between the estimators of the initial value  $\vec{a}$ , given  $\vec{x}(t)$ , in the class and in the full distribution. This difference is typically a function that decreases with the time of the backward process. This suggests to use a non-linear CFG of the form

$$\begin{aligned} \vec{S}_t^{\text{RPL}}(\vec{x}, c) &= \vec{S}_t(\vec{x}, c) + \omega \left[ \vec{S}_t(\vec{x}, c) - \vec{S}_t(\vec{x}) \right] |\langle \vec{a} \rangle_{\vec{x}, c} - \langle \vec{a} \rangle_{\vec{x}}|^\gamma \\ &= \vec{S}_t(\vec{x}, c) + \omega \left[ \vec{S}_t(\vec{x}, c) - \vec{S}_t(\vec{x}) \right] \left| \vec{S}_t(\vec{x}, c) - \vec{S}_t(\vec{x}) \right|^\gamma s(t)^\gamma \sigma(t)^{2\gamma} \end{aligned} \quad (31)$$

with positive  $\gamma$ . As we will show in Figures 12-13, this non-linear guidance term has interesting performance in terms of combining a rapid drift toward the desired class  $c$  at early stages of the backward process together with small bias in the finite distribution in finite dimensional problems.

<sup>4</sup>For large values of  $x \cdot (\vec{\mu}_1 \pm \vec{\mu}_2) e^{-t}/\Gamma_t$ , we utilized the *log-sum-exp trick* to calculate the value of the fraction.

The behavior of both versions is further displayed in Figure 14: both non-linear versions can yield smaller bias at  $t = 0$ . Furthermore, Figure 14 also displays additional experiments highlighting the benefits of non-linear versions.

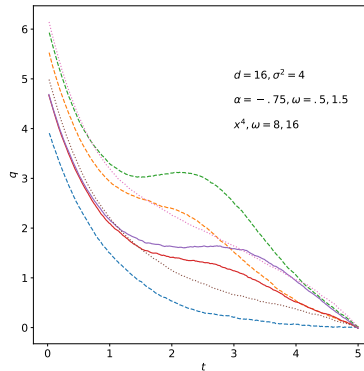


**Figure 12**  $\langle q \rangle$  versus time in the Gaussian binary mixture with  $d = 16$  and  $\sigma^2 = 4$ . The dashed line are obtained by the standard linear CFG with  $\omega = 0, 8, 16$  from bottom to top. The dotted line are obtained with the Power-Law non-linear scheme  $f(x) = \omega x^{-.75}$  with  $\omega = .5, 1.5$  from bottom to top. The full lines are obtained with the non-linear guidance of Eq.(31) with  $\gamma = 4$  and  $\omega = 8, 16$  from bottom to top. The Rescaled Power-law non-linear scheme departs from  $q = 0$  at large time on a trajectory similar to the linear scheme and to the Power-Law non-linear scheme. But it gives a smaller bias at  $t = 0$ .

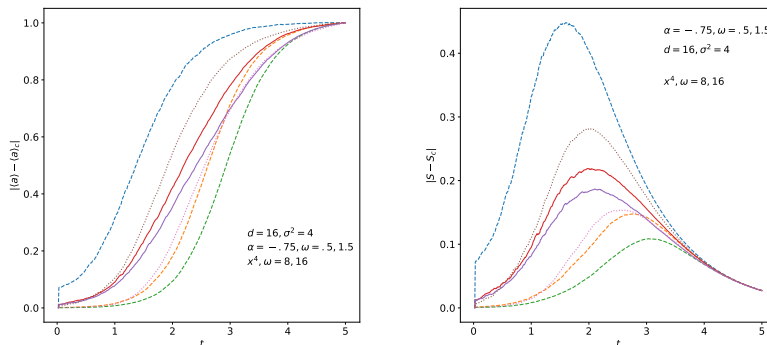


**Figure 13** We perform the same experiment as in Fig. 12. We plot on the left the value of  $|\langle \vec{a} \rangle_{\vec{x}=\vec{0},c} - \langle \vec{a} \rangle_{\vec{x}=\vec{0}}|$ , on the right the value of  $|S_t(\vec{x}, a) - S_t(\vec{x})|$ , with the same linestyle and color code as in Fig. 12.

## G Applying Classifier-Free Guidance in a limited interval

In Kynkäänniemi et al. (2024), the authors propose to apply standard CFG within a limited time interval. Their method therefore applies the following schedule for the classifier parameter  $\omega$ :

$$w(\sigma_t) = \begin{cases} w & \text{if } \sigma_t \in (t_1, t_2] \\ 0 & \text{otherwise.} \end{cases}$$

Here,  $\sigma_t$  represents the noise level at time  $t$  of the forward process. Therefore,  $t_1$  and  $t_2$  correspond to points in the sampling chain in which they disable and enable guidance respectively. These are treated as additional

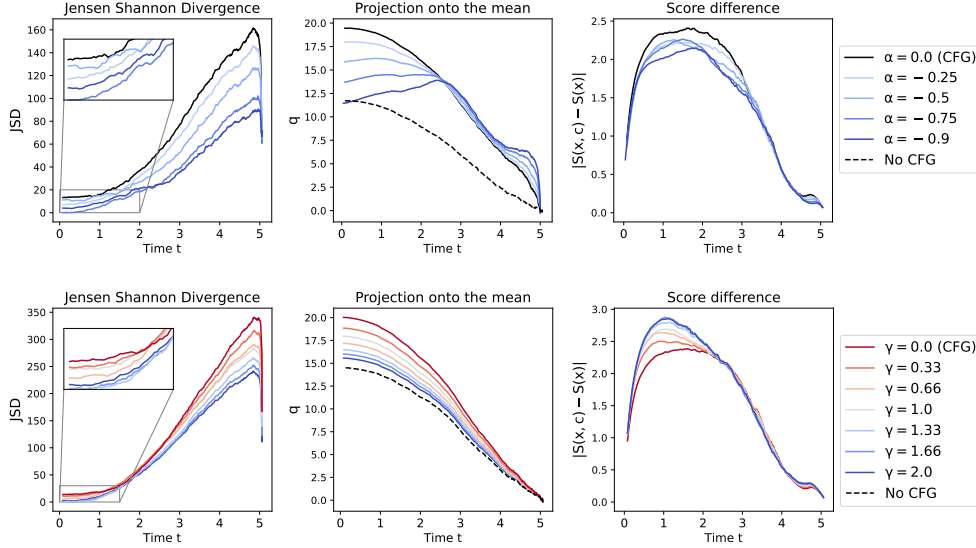


**Figure 14** Real-world experiments using DiT/XL-2 (Peebles and Xie, 2023) trained on ImageNet-1000 (Deng et al., 2009): randomly selected class with  $\omega = 4$ , using DDPM (Ho et al., 2020) with 250 sampling steps, averaged over 25 samples. **First column:** Power-Law CFG. **Second column:** Rescaled Power-Law CFG (31). **Left column:** Jensen-Shannon Divergence between the embedded data points corresponding to randomly selected class and the generated samples as a function of reverse time  $\tau$ . **Middle column:** mean dot product of the normalized class centroid and the diffusion trajectories  $\vec{x} \cdot \vec{c}_i / \|\vec{c}_i\|$  (both in the latent space) as a function of reverse time  $\tau$ . **Right column:** Evolution of the distance between conditional and unconditional scores. From all three plots, we can see that using first (second) version of non-linear CFG with  $\alpha < 0$  ( $\gamma > 0$ ) results in paths that have smaller JSD, estimated as in Wang et al. (2009), throughout the whole trajectory and smaller overshoot of the distribution’s mean at  $\tau = 0$ . We can also see that the score difference  $|S_\tau(x, c) - S_\tau(x)|$  has the same qualitative behavior as in numerical simulations of Gaussian mixtures.

hyperparameters over which grid search is performed (alongside  $\omega$ ). The standard CFG is recovered with  $t_1 = 0$  and  $t_2 = \infty$ .

By performing the reparameterization introduced in Section D.1, we can map  $t_1$  and  $t_2$  (obtained by minimizing the FID and  $FD_{DINOv2}$  objectives respectively) to our timescale. The findings are shown in Figure 15: on the left, the hyperparameter configuration that minimizes the FID objective is obtained with  $\omega = 2.5$ ,  $t_1 = 0.34$  and  $t_2 = 1.04$ . The hyperparameter configuration that minimizes the test  $FD_{DINOv2}$  loss corresponds to  $\omega = 4.0$ ,  $t_1 = 0.45$  and  $t_2 = 1.23$ .

Our findings suggest that stopping CFG just before the score difference begins to decay may coincide with the speciation time. Interestingly, delaying the start of guidance appears to have a positive impact on the FID metric, despite theoretical expectations. We attribute this phenomenon to imperfect score estimation, particularly at high noise levels, which deviates from our assumption of a perfect score estimator. Further investigation of this observation is left for future research.

Additionally, we experimented with stopping guidance after the score difference becomes significantly small, as theory suggests this should not affect generation in Regime II and is more computationally efficient. While this held true in practice, it was only observed in the EDM2 framework, whereas other scores remained substantial until almost the end, as shown in Figures 5 and 15.

## G.1 Estimating the starting and stopping point

As described in the main manuscript, we employ an initial set of warm-up runs to estimate  $t_1$  and  $t_2$ . Specifically, we utilize the average of 1,000 paths to determine the first timestep at which the score difference  $|S_t(\vec{x}, c) - S_t(\vec{x})|$  surpasses its mean value, thereby obtaining  $t_2$ . Subsequently, we identify the timestep corresponding to the mode of the curve, marking the onset of decay, which yields  $t_1$ . A comparison between

the  $t_1$  and  $t_2$  values obtained through hyperparameter optimization and our proposed heuristic is presented in Figure 15.

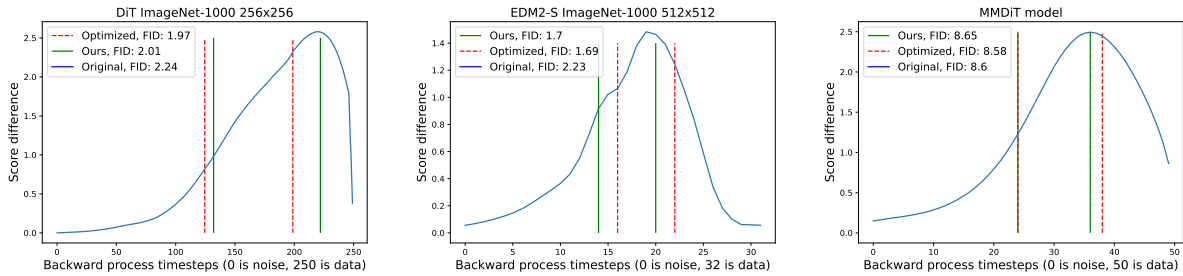


**Figure 15** Timescales  $t_2$  (left) and  $t_1$  (right) at which Standard CFG is turned on and off respectively. Timesteps obtained through hyperparameter sweep are portrayed with red dashed lines, and using our heuristic in green solid lines. Notably, our heuristic achieves comparable performance to the baseline for DiT/XL-2 and EDM2-S, while requiring two less hyperparameters. This reduction in hyperparameters can be particularly advantageous in computationally expensive applications, such as diffusion models. Our experiments with the MMDiT (diffusion) model yielded smaller improvement in the FID, whereas with the MDTv2 architecture experiments revealed that limiting the guidance interval did not yield significant benefits, even after conducting an exhaustive grid search over  $t_1$  and  $t_2$ .

## H Images by DiT/XL-2 (256x256)

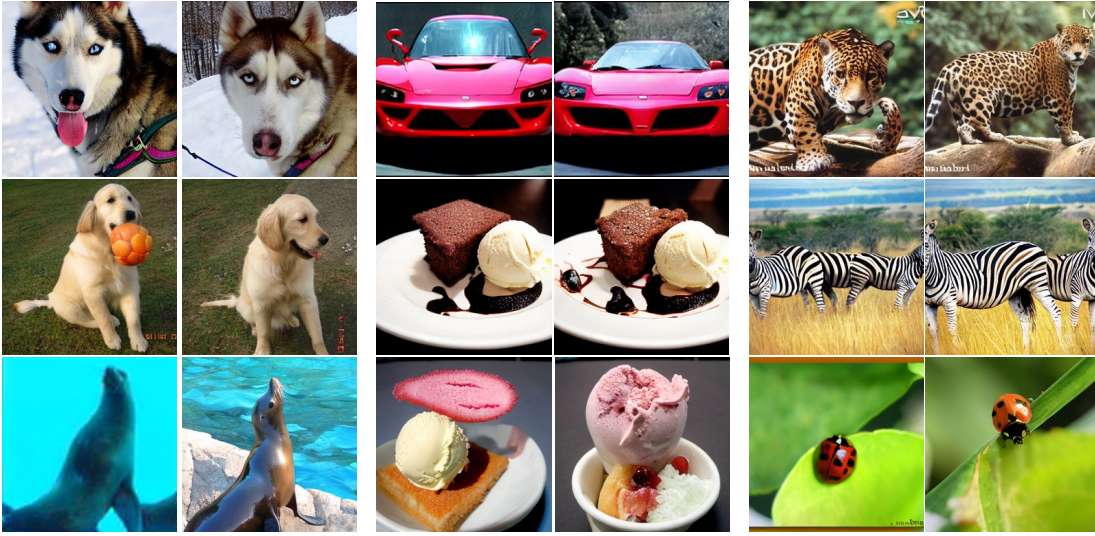


**Figure 16** Additional examples generated by DiT/XL-2 using Standard CFG ( $\omega = 4$ ) and Power-Law CFG ( $\omega = 4, \alpha = 0.15$ ). Image pairs start from the same noise (same seed). The resulting pairs represent Standard CFG on the left and Power-Law CFG on the right.



**Figure 17** Images generated conditioned on the class *pineapple* using Standard CFG ( $\omega = 4$ ).



**Figure 18** Images generated conditioned on the class *pineapple* using Power-Law CFG ( $\omega = 4, \alpha = 0.15$ ).



**Figure 19** Images generated conditioned on the class *water ouzel, dipper* using Standard CFG with  $\omega = 4$ .



**Figure 20** Images generated conditioned on the class *water ouzel, dipper* using Power-Law CFG with  $\omega = 4, \alpha = 0.15$ .



**Figure 21** Images generated conditioned on the class *vine snake* using Standard CFG with  $\omega = 4$ .



**Figure 22** Images generated conditioned on the class *vine snake* using Power-Law CFG with  $\omega = 4, \alpha = 0.15$ .

# I Images by MMDiT model (diffusion objective, resolution 512x512)



**Figure 23** Images generated conditioned on the textual prompt *Glowing mushrooms in a dark forest.* using Standard CFG with  $\omega = 3$  (top two rows) and Power-Law CFG with  $\omega = 3, \alpha = 0.1$  (bottom two rows).

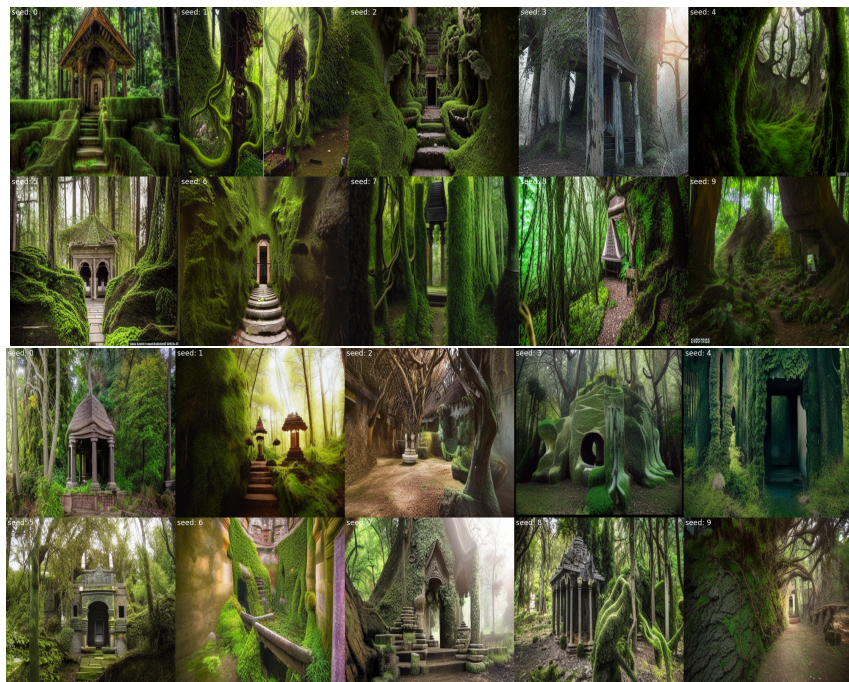


**Figure 24** Images generated conditioned on the textual prompt *Mysterious, abandoned temple with vines and moss* using Standard CFG with  $\omega = 3$  (top two rows) and Power-Law CFG with  $\omega = 3, \alpha = 0.1$  (bottom two rows).



**Figure 25** Images generated conditioned on the textual prompt *Glowing, ethereal fireflies in a summer evening* using Standard CFG with  $\omega = 3$  (top two rows) and Power-Law CFG with  $\omega = 3, \alpha = 0.1$  (bottom two rows).

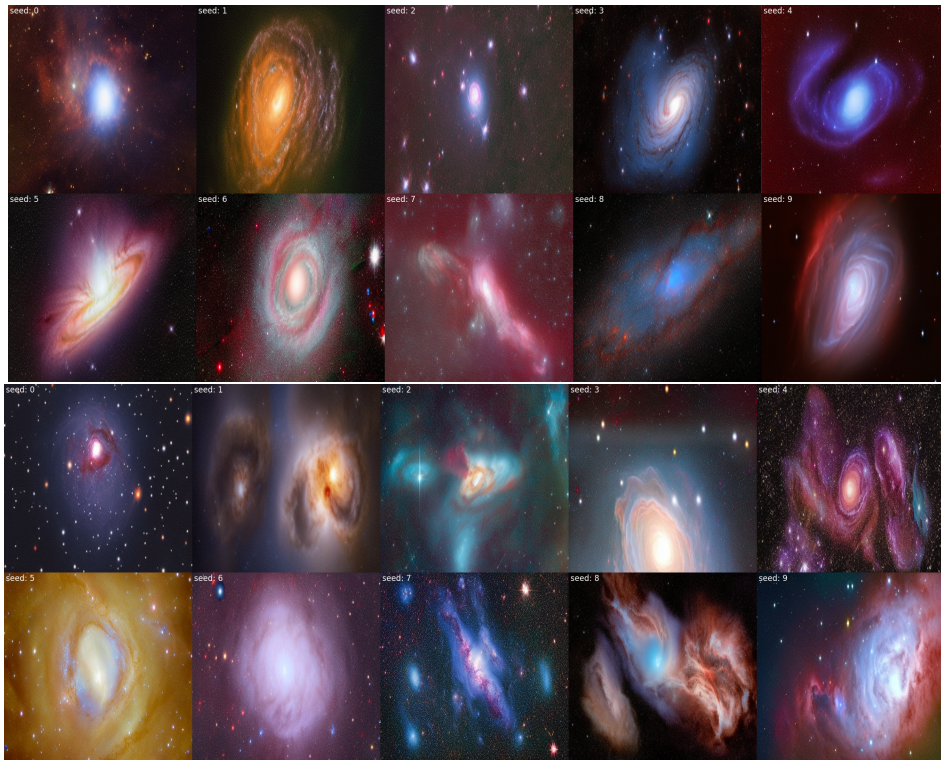


**Figure 26** Images generated conditioned on the textual prompt *Stunning, breathtaking view of a galaxy or nebula* using Standard CFG with  $\omega = 3$  (top two rows) and Power-Law CFG with  $\omega = 3, \alpha = 0.1$  (bottom two rows).